Electronic Supplementary Material (ESI) for Dalton Transactions.

Hexahydroxytriphenylene for the Synthesis of Group 13 MOFs – a New Inorganic Building Unit in a β-cristobalite Type Structure

S. Leubner,[a] V. Bengtsson,[b] A. K. Inge,[b] M. Wahiduzzaman,[c] F. Steinke,[a] A. Jaworski,[b] H. Xu,[b] S. Halis,[a] P. Rönfeldt,[a] H. Reinsch,[a] G. Maurin,[c] X. Zou[b] and N. Stock[a]*

[a] *S. Leubner, F. Steinke, S. Halis, P. Rönfeldt, H. Reinsch, N. Stock*
Institute für Anorganische Chemie, Christian-Albrechts-Universität, Max-Eyth-Straße 2, D 24118 Kiel, Germany.

[b] *V. Bengtsson, A. K. Inge, A. Jaworski, H. Xu, X. Zou*
Department of Materials and Environmental Chemistry, Stockholm University, SE-106 91 Stockholm, Sweden.

[c] *M. Wahiduzzaman, G. Maurin*
Institut Charles Gerhard Montpellier,
UMR-5253 Universite Montpellier CNRS ENSCM
Place E. Bataillon 34095, Montpellier cedex 05, France

1. Redox properties of 2,3,6,7,10,11-hexahydroxytriphenylen H_6HHTP

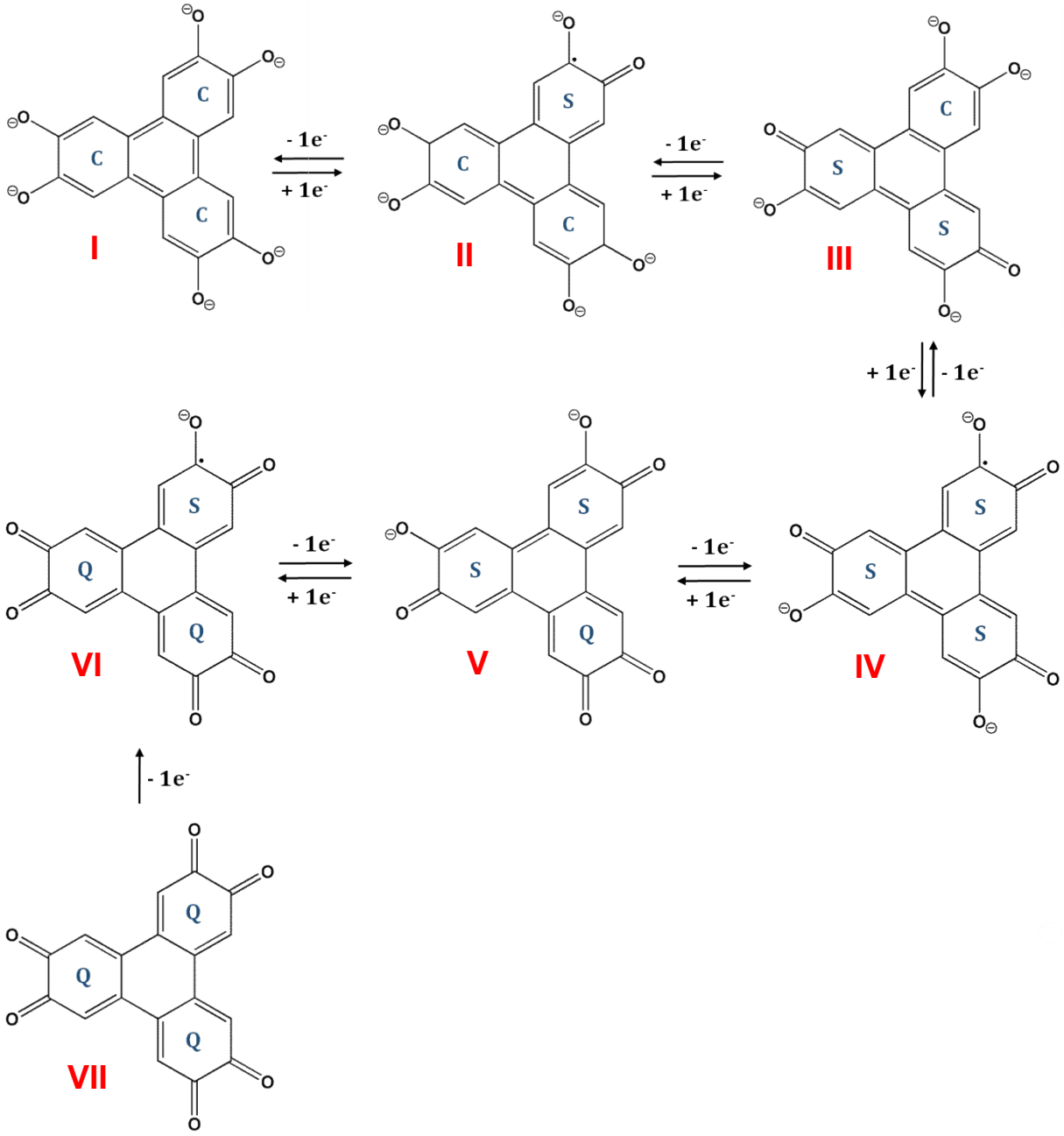

Fig. S1.1. Redox and acid-base chemistry of H_6HHTP. The fully deprotonated $HHTP^{6-}$ ion can exist in seven oxidation states containing the dianionic catecholate (C), monoanionic semiquinone (S) or neutral quinone (Q) redox states: $HHTP^{6-}$ (CCC, **I**), $HHTP^{\bullet 5-}$ (CCS, **II**), $HHTP^{4-}$ (CSS, **III**), $HHTP^{\bullet 3-}$ (SSS, **IV**), $HHTP^{2-}$ (SSQ, **V**), $HHTP^{\bullet 1-}$ (SQQ, **VI**) and $HHTP^{0}$ (QQQ, **VII**).

2. Experimental

Chemicals: All chemicals, aluminum perchlorate $Al(ClO_4)_3 \cdot 9H_2O$, aluminum chloride $AlCl_3 \cdot 6H_2O$, gallium nitrate $Ga(NO_3)_3 \cdot xH_2O$, the linker 2,3,6,7,10,11-hexahydroxytriphenylene ($C_{18}H_6(OH)_6$, H_6HHTP) and the solvent *N*'*N*-dimethylformamide (C_3H_7NO, DMF), were used as obtained. Deionized water was treated with nitrogen gas which was passed through at room temperature for 1 h in order to reduce the concentration of dissolved oxygen molecules.

Characterization Methods:

PXRD data were collected in transmission geometry using a STOE STADI P diffractometer (Cu-Kα_1 radiation, λ = 1.5406 Å) equipped with a Mythen detector. Lattice parameters were determined and refined using Topas Academic.[1] Structural models were set up by using the indexed cell parameters and optimizing the models by force-field based energy minimizations using the universal force field[2] as implemented in the Forcite module in the Materials Studio software.[3]

Thermogravimetric (TG) measurements were carried out with a heating rate of 2 °C min^{-1} under air (75 cm^3 min^{-1}) using a NETSCH STA 409 CD analyzer.

Elemental analyses (C, H, N, S) were performed on a EuroVector EuroEA elemental analyzer.

MIR spectra were recorded on a Bruker ALPHA-P FT-IR spectrometer in the spectral range 4000-400 cm^{-1} at room temperature.

EPR spectra were collected at room temperature on a Bruker EMX*plus* spectrometer with a PremiumX microwave bridge equipped with a dual mode cavity (Bruker ER-4116DM).

Sorption measurements were carried out using a BELSORP-max instrument (BEL JAPAN INC.). The samples were activated at 170 °C under dynamic vacuum (10^{-2} kPa) for 12 h. Nitrogen sorption measurements were performed at 77 K and measurements using carbon dioxide at 298 K. Specific surface areas were determined from the N_2 adsorption isotherms using the BET method, as described in the literature by Rouquerol et al.[4] Micropore volumes were calculated from the N_2-adsorption isotherm at p/p_0 = 0.5. The theoretical micropore volume was calculated using the program PLATON.[5]

Collection of continuous rotation electron diffraction (cRED) data was done on a 200kV JEOL JEM 2100 LaB_6 transmission electron microscope (TEM) with a TimePix hybrid pixel detector[6]. The detector was controlled using the vendor control software SoPhy and manual trackback to keep the crystal within the aperture. Prior to data collection the crystals used for structure determination were crushed and diluted in ethanol and deposited on a lacy carbon grid. Further parameters are summarized in Tab. S2.1.

Tab. S2.1. cRED data collection parameters.

Parameter	Setting
Rotation range	120.6°
Rotation speed	0.46°s^{-1}
Exposure time	0.5s
Temperature	98K
Holder	Gatan 914 cooling holder

The MAS NMR experiments were performed at the magnetic field B_0 = 14.1 T (600.12 MHz ^{1}H Larmor frequency) and MAS rate ν_r = 60.00 kHz on a Bruker Avance-III spectrometer equipped with 1.3 mm MAS probehead. Proton acquisitions involved rotor-synchronized, double-adiabatic spin-echo sequence with 90° 1.2 μs excitation pulse followed by two 50.0 μs tanh/tan high-power adiabatic pulses (SHAPs) with 5 MHz frequency sweep.[7,8,9] All pulses operated at the nutation frequency ν_{nut} = 210 kHz. 128 signal transients with 1 s relaxation delays were accumulated for each spectrum. The ^{27}Al MAS NMR spectrum was collected with short, 0.25 μs excitation pulse operated at 100 kHz at ν_{nut} = 110 kHz. 65536 scans with 0.5 s pulse delay were accumulated. ^{1}H-{^{27}Al} TRAPDOR[10] NMR experiments with recoupling pulse applied on ^{27}Al channel at ν_{nut} = 110 kHz (and duration τ_{rec}) were performed to probe proton-aluminum contacts in the material. In such experiment the heteronuclear dipolar interaction between protons and aluminum is recoupled, with the interaction strength proportional to the internuclear distance.

3. Synthesis of $((CH_3)_2NH_2)_2[Al_3O(HHTP)(HHTP^{\bullet})]\cdot 0.5DMF\cdot 18H_2O$ and $((CH_3)_2NH_2)_2[Ga_3O(HHTP)(HHTP^{\bullet})]\cdot 14.5H_2O$

The two title compounds $((CH_3)_2NH_2)_2[Al_3O(HHTP)(HHTP^{\bullet})]\cdot 0.5DMF\cdot 18H_2O$ (Al-CAU-42) and $((CH_3)_2NH_2)_2[Ga_3O(HHTP)(HHTP^{\bullet})]\cdot 14.5H_2O$ (Ga-CAU-42) were discovered using our high-throughput (HT) methodology.[11] The reactor blocks containing 24 Teflon inserts with V_{max} = 2 ml were employed. The same set-up was also used for the synthesis optimization.
In this study the molar ratios of Al^{3+}/Ga^{3+} : H_6-HHTP was varied and DMF as well as H_2O were used as solvent. After a crystalline product was obtained the DMF to water ratio was varied. In addition, the reaction time and temperature were also optimized between 24 to 72 h and 120 - 150 °C. Details of the HT investigations are summarized in Figure 3.1.

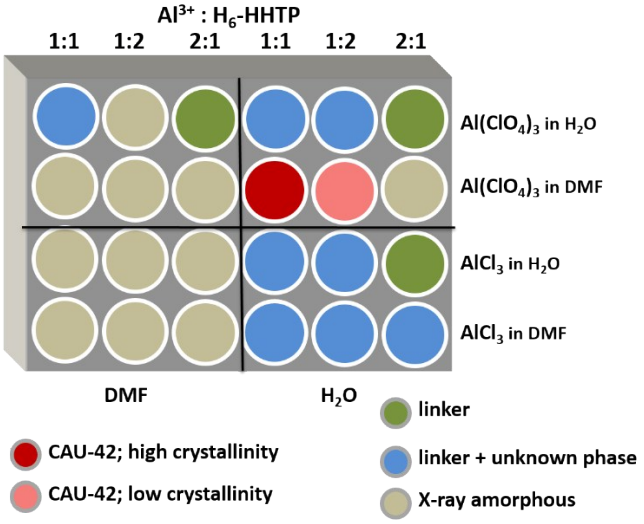

Fig. S3.1. Schematic representation of the high-throughput study that led to the discovery of $((CH_3)_2NH_2)_2[Al_3O(HHTP)(HHTP^{\bullet})]\cdot 0.5DMF\cdot 18H_2O$ (Al-CAU-42). The molar ratios metal to linker as well as the Al^{3+} salt and the main solvent (DMF or H_2O) were varied. Highly crystalline CAU-42 is obtained when $Al(ClO_4)_3$ and a mixture of DMF and H_2O are used.

As shown in the schematic representation of the high-throughput reaction, the molar metal to linker ratio (2:1, 1:1 and 1:2) as well as the Al^{3+} salt (chloride or perchlorate) and the main solvent (DMF or H_2O) were varied. CAU-42 was obtained only in two cases. A product of low crystallinity is obtained when $Al(ClO_4)_3$ and a mixture of DMF and H_2O are used. Highly crystalline CAU-42 is obtained when a metal to linker ratio of 1:1 is used.

Optimized syntheses:
$((CH_3)_2NH_2)_2[Al_3O(HHTP)(HHTP^{\bullet})]\cdot 0.5DMF\cdot 18H_2O$: 32.4 mg (0.1 mmol) H_6HHTP, 400 µL (0.1 mmol) $Al(ClO_4)_3\cdot 9H_2O$ (0.25 M in DMF), 400 µL DMF and 200 µL H_2O were mixed in a 2 ml Teflon reactor and transferred into the HT reactor.
$((CH_3)_2NH_2)_2[Ga_3O(HHTP)(HHTP^{\bullet})]\cdot 14.5H_2O$: 32.4 mg (0.1 mmol) H_6HHTP, 200 µL (0.1 mmol) $Ga(NO_3)_3\cdot x\,H_2O$ (0.5 M in DMF), 600 µL DMF and 200 µL H_2O were mixed in a 2 ml Teflon reactor and transferred into the HT reactor.
The reactors were placed in a conventional oven (forced air circulation) and heated for 48 h at 150 °C. The resulting products were filtrated and washed with DMF, ethanol and dichloromethane. Afterwards the products were redispersed in 1.5 mL dichloromethane and centrifuged again. This redispersion/centrifugation process was repeated ten times. Due to moisture and air sensitivity the microcrystalline products were stored in dichloromethane. For

characterization samples were dried in air. Both compounds are stable in dichloromethane and under N_2 atmosphere. Synthesis scale-up is possible using the tenfold amounts.

4. Crystal structure determination

4.1 Pawley refinement

The PXRD patterns of both title compounds, Al- and Ga-CAU-42, were indexed and the lattice parameters were refined using the Pawley method[12] as implemented in the program Topas.[13] The results of the Pawley fits of the purified compounds are shown in Figure S4.1.1 and Table S4.1.1.

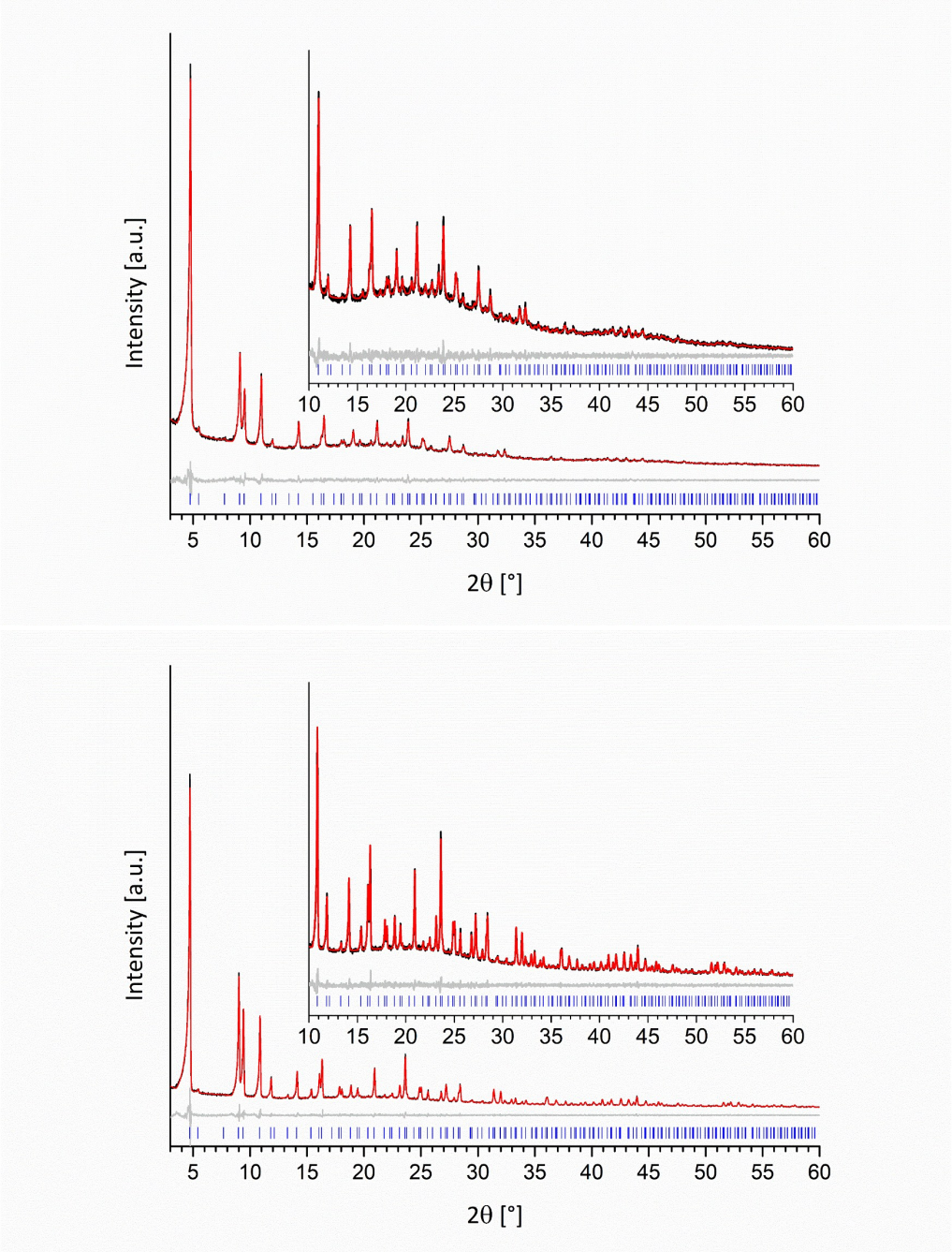

Fig. S4.1.1. Pawley fits of purified Al-CAU-42 (top) and Ga-CAU-42 (bottom). The observed PXRD pattern (λ = 1.5401 Å) is shown in black, the calculated in red and the difference (observed - calculated) of both patterns is given in grey. The allowed positions of the reflections are given as blue tics.

Figure S4.1.2 and Table S4.1.1 contain the results of the Pawley fits of the activated compounds (reduced pressure, 170 °C, 12 h). The crystallinity of the compounds is negatively affected by the thermal treatment.

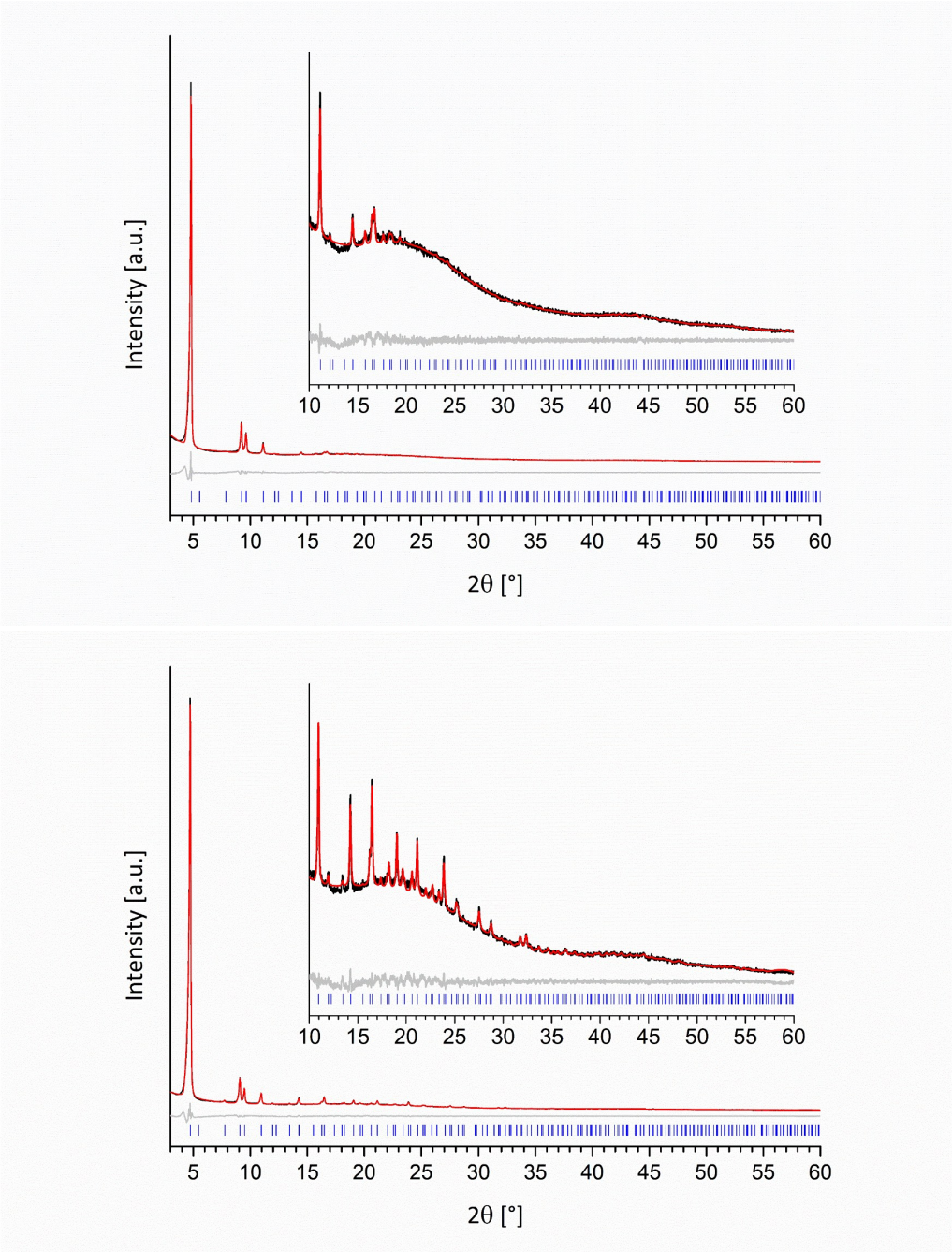

Fig. S4.1.2. Pawley fits of the thermally activated compounds (reduced pressure, 170 °C, overnight) Al-CAU-42 (top) and Ga-CAU-42 (bottom). The observed PXRD patterns (λ = 1.5401 Å) are shown in black, the calculated in red and the difference (observed - calculated) of both patterns are given in grey. The allowed positions of the reflections are given as blue tics.

Tab. S4.1.1. Results of the Pawley fits of purified (top) and activated (bottom) Al- and Ga-CAU-42.

	$((CH_3)_2NH_2)_2[Al_3O(HHTP)(HHTP^{\bullet})]\cdot 0.5DMF\cdot 18H_2O$	**$((CH_3)_2NH_2)_2[Ga_3O(HHTP)(HHTP^{\bullet})]\cdot 14.5H_2O$**
Crystal system	cubic	cubic
$a = b = c$ / Å	32.2703(15)	32.6358(4)
V / Å^3	33605(4)	34760(1)
Space group	*F*23	*F*23
R_{wp}	3.4 %	3.9 %
GoF	2.1	2.3
	$((CH_3)_2NH_2)_2[Al_3O(HHTP)(HHTP^{\bullet})]$ (activated at 170 °C)	**$((CH_3)_2NH_2)_2[Ga_3O(HHTP)(HHTP^{\bullet})]$** (activated at 170 °C)
Crystal system	cubic	cubic
$a = b = c$ / Å	31.7302(40)	32.2206(24)
V / Å^3	31946(12)	33450(7)
Space group	*F23*	*F23*
R_{wp}	4.3 %	4.1 %
GoF	1.4	2.3

4.2 Structure modelling

To create a basic understanding of the appearance and network connectivity of CAU-42, initially, structure modeling was carried out. A suitable structure model was obtained from 3D MOF structures reported in the literature that contain large linker molecules which are geometrically similar to H_6HHTP and crystallize in a cubic space group with similar lattice parameters. These criteria lead to the two compounds MOF-500[14] with the composition $(DMA)_8[(Fe_3O)_4(SO_4)_{12}(BPDC)_6(BPE)_6]$ (DMA^+ = dimethylammonium, $BPDC^{2-}$ = 4,4'-biphenyldicarboxylate, BPE = *cis*-1,2-bis-4-pydridylethan) and PCN-777 (PCN = porous coordination network)[15] ($[Zr_6(O)_4(OH)_{10}(H_2O)_6(TATB)_2]$, $TATB^{3-}$ = 4,4',4''-*s*-triazin-2,4,6-triyl-tribenzoate). Both compounds crystallize in a cubic space group and exhibit a porous β-cristobalite[16] type network.

Starting from the crystal structures of MOF-500 and PCN-777 and the lattice parameters obtained from the Pawley fit of the purified compounds, a structure model was set up using the program Materials Studio[3]. The molar metal to linker ratio was fixed to a value of 3 to 2 as determined from the thermogravimetric measurements. The organic linker molecules ($TATB^{3-}$) were replaced by the planar $HHTP^{6-/\bullet 3-}$ ions (the presence of the radical ions was confirmed by ESR measurements (Fig. S5.1)) and various IBUs composed of AlO_6 polyhedra were tested. The structural models were geometry optimized at the force field level using the module Forcite as implemented in Materials Studio. The three plausible models **A**, **B**, and **C** were thus obtained (Fig. S4.2.1). The final structure was determined via continuous rotation electron diffraction (cRED) and it was shown that the actual IBU is very similar to IBU **B** (see section Continuous rotation electron diffraction (cRED), Fig. S4.3.4). While the structure model postulated an alternation of mono- and bidentate coordinating linker molecules together with additional water ligands around the Al^{3+} ions, the final structure only exhibits bidentate coordinated linker molecules and no water ligands. The absence of water ligands around the Al^{3+} centers was further confirmed via ^{1}H-^{27}Al-TRAPDOR (transfer of populations in double resonance) solid-state NMR experiments (Fig. S10.1b).

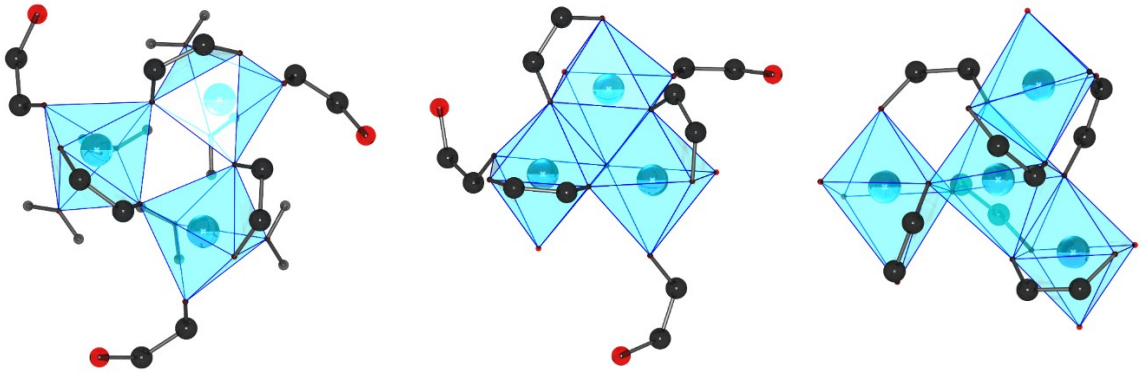

Fig. S4.2.1. Structurally plausible IBUs **A**, **B**, and **C** containing corner and/or edge sharing AlO_6 polyhedra as obtained from force field calculations. The final IBU as determined via cRED is very similar to IBU **B** (continuous rotation electron diffraction (cRED)). The MO_6 polyhedra are represented in light blue. Carbon: black, oxygen: red, hydrogen: light grey.

4.3 Continuous rotation electron diffraction (cRED)

The cRED data were processed and integrated using DIALS[17] and scaled using aimless[18]. ShelxT[19] and shelxl[20] (through shelXle[21]) were used for structure solution and refinement, respectively (Tab. 4.3.1).

Tab. S4.3.1. Statistics of the Al-CAU-42 structure refinement against cRED data. DFIX, DANG and FLAT restraints were used to keep the HHTP linker molecule in a chemically reasonable shape.

Parameter	Value
Space group	*F*23
Unit cell parameter a	33.126(8) Å
Resolution	1.00 Å
Mean *I/σ*	4.4
Reflections total/unique	22410/1715
Completeness	100 %
Multiplicity	13.1
CC(1/2) in outer shell	0.761
Resolution for outer shell	1.07 - 1.00 Å
Parameters/restraints	76/56
GooF	1.043
R1 for 1221*Fo> 4σ(Fo)/all*	0.2196/0.2545

In order to further confirm the model due to the relatively high R-values of the cRED data, structure refinement of an activated Al-CAU-42 sample was performed against PXRD data using TOPAS Academic 6[13] (Fig. S4.3.1, Tab. S4.3.2). The space group *F*23 was selected in order to distinguish the two disordered positions that one of the two symmetry independent linker molecules occupy. The linker molecules were modelled using a Z-matrix, in order to maintain reasonable bond distances and angles. Distance and angle restraints were applied to Al-O and O-Al-O, respectively.

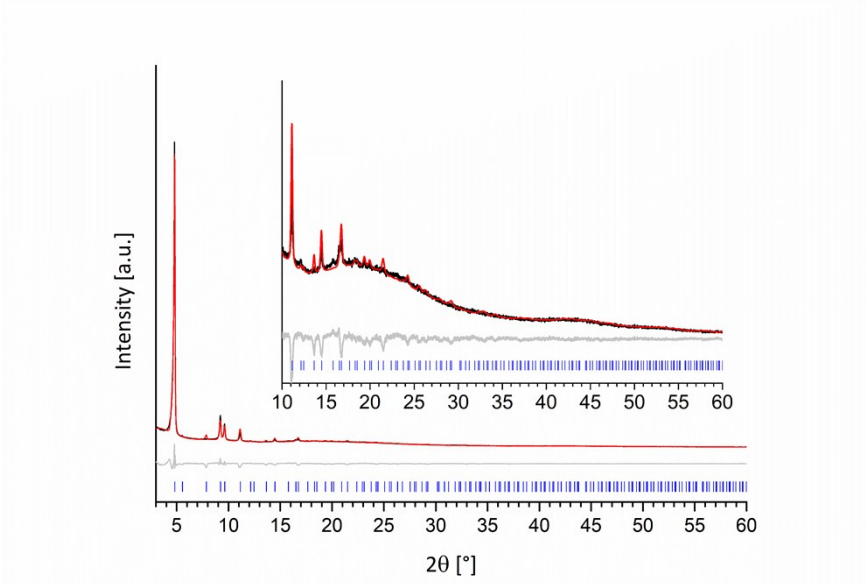

Fig. S4.3.1. Rietveld refinement of thermally activated Al-CAU-42 (reduced pressure, 170 °C, overnight). The observed PXRD pattern (λ= 1.5401 Å) is shown in black, the calculated in red

and the difference (observed - calculated) of both patterns is given in grey. The allowed positions of the reflections are given as blue tics.

Tab. S4.3.2. Statistics of the Al-CAU-42 structure refinement against PXRD data of an activated sample.

Parameter	Value
Space group	*F*23
Unit cell parameter a	31.732(4) Å
Cell volume	3195(14)
R_{bragg}	2.76
R_{wp}	6.30 %
GOF	1.76

A *β*-cristobalite type network was obtained as expected from structure modelling. The network type is characterized by two types of corner-sharing supertetrahedra. The IBU represents a trimer of AlO_6 octahedra which connects to six HHTP ($HHTP^{6-}$ and $HHTP^{\bullet 3-}$) linker ions. (Fig. S4.3.2).

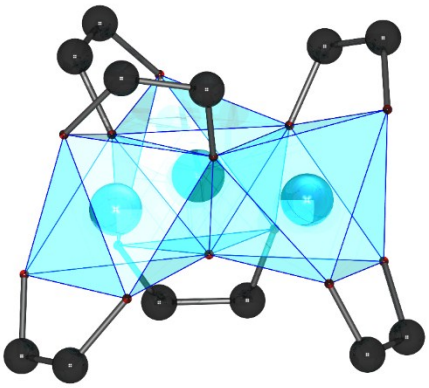

Fig. S4.3.2. Trimeric IBU of Al-CAU-42. Fragments of the catecholate subunits are displayed in order to clarify coordination environment and connectivity. AlO_6 polyhedra are represented in light blue. Aluminum: light blue, Carbon: black, Oxygen: red.

Each AlO_6 octahedron shares two of its edges with the remaining two octahedra. Five of the six coordinated oxygen atoms per Al^{3+} ion originate from the phenolate groups of the linker molecules while the sixth is an μ_3-O^{2-} ion located slightly below the center of gravity of the trimer. The catecholate subunits of the linker molecules coordinate to the Al^{3+} ions in two different bidentate ways. They can either coordinate through one terminal and one µ-oxygen atom (Fig. S4.3.2, upper half of the trimeric unit) or exclusively through terminal oxygen atoms (Fig. S4.3.2, lower half of the trimeric unit). From the coordination scheme in the upper half of the trimeric unit, two disordered positions arise for the corresponding linker molecules. Besides coordinating to one µ-oxygen atom, they can either coordinate to the left or right neighboring terminal position (Fig. S4.3.3). The described IBU deviates only slightly from the IBU postulated in model **B** (Fig. S4.3.4, also see Fig. S4.2.1 in section Structure modelling).

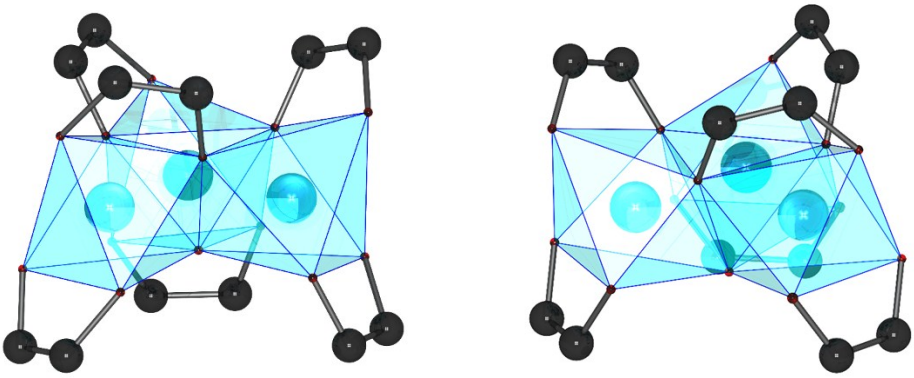

Fig. S4.3.3. Different coordination schemes arising from the two disordered positions of the linker molecules which connect to the upper half of the trimeric unit. Fragments of the catecholate subunits are displayed in order to clarify coordination environment and connectivity. AlO_6 polyhedra are represented in light blue. Aluminum: light blue, Carbon: black, Oxygen: red.

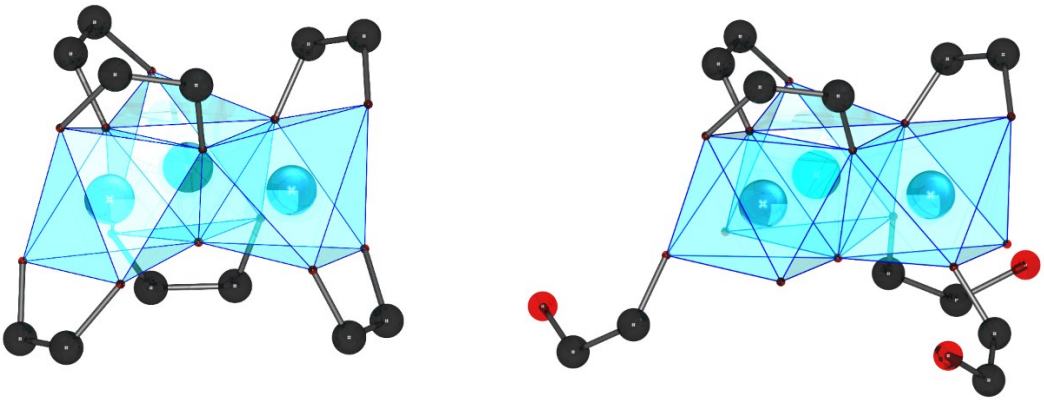

Fig. S4.3.4. Trimeric IBU of Al-CAU-42 as determined from cRED experiments (left) in comparison with the IBU of structure model **B** (right, see Structure modelling). Fragments of the catecholate subunits are displayed in order to clarify coordination environment and connectivity. AlO_6 polyhedra are represented in light blue. Aluminum: light blue, Carbon: black, Oxygen: red.

Each $HHTP^{6-/3\bullet-}$ ion is coordinated to three trimeric units. The interconnection of the trimeric units leads to the formation of two types of supertetrahedra: a smaller and a larger supertetrahedron with an inner pore diameter of 4.8 and 6 Å, respectively (Fig. S4.3.5).

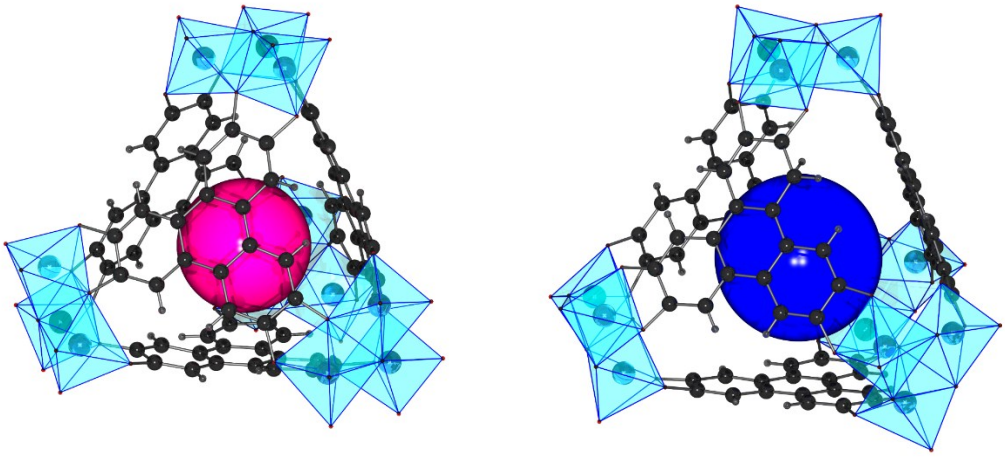

Fig. S4.3.5. Smaller (left) and larger supertetrahedron (right) of Al-CAU-42 formed by the interconnection of trimeric units. Pink and blue spheres with a diameter of 4.8 and 6 Å, respectively, represent the pore space of the supertetrahedra. AlO_6 polyhedra are represented in light blue. Aluminum: light blue, Carbon: black, Oxygen: red, Hydrogen: light grey.

The connectivity of the supertetrahedra creates a *β*-cristobalite type framework. While in *β*-cristobalite the O atoms link the Si atoms, in the supertetrahedra of CAU-42 the connection to the three-dimensional framework is accomplished through the IBUs. The relationship between these two structures in demonstrated in Fig. S4.3.6.

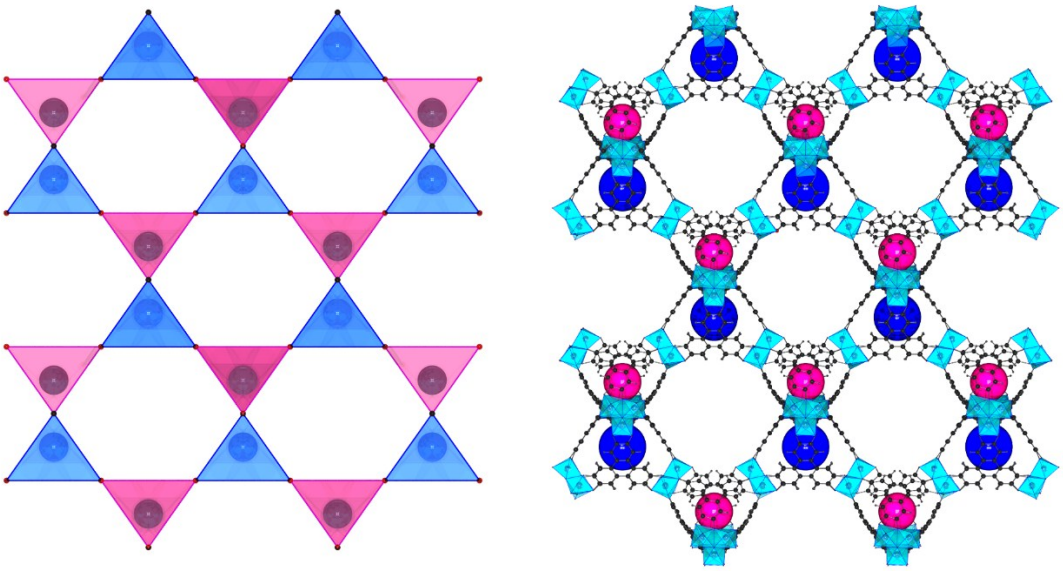

Fig. S4.3.6. View of the crystal structure of *β*-cristobalite (left)[16] and Al-CAU-42 (right) along [101]. For comparison: The cell volume in *β*-cristobalite is ca. 360 $Å^3$, while it is ca. 34000 $Å^3$ for Al-CAU-42. AlO_6 polyhedra are represented in light blue. Aluminum: light blue, Silicon: dark green, Carbon: black, Oxygen: red, Hydrogen: light grey.

The arrangement of supertetrahedra of Al-CAU-42 creates a major tetrahedral pore with an approximate diameter of 16 Å (Fig. S4.3.7).

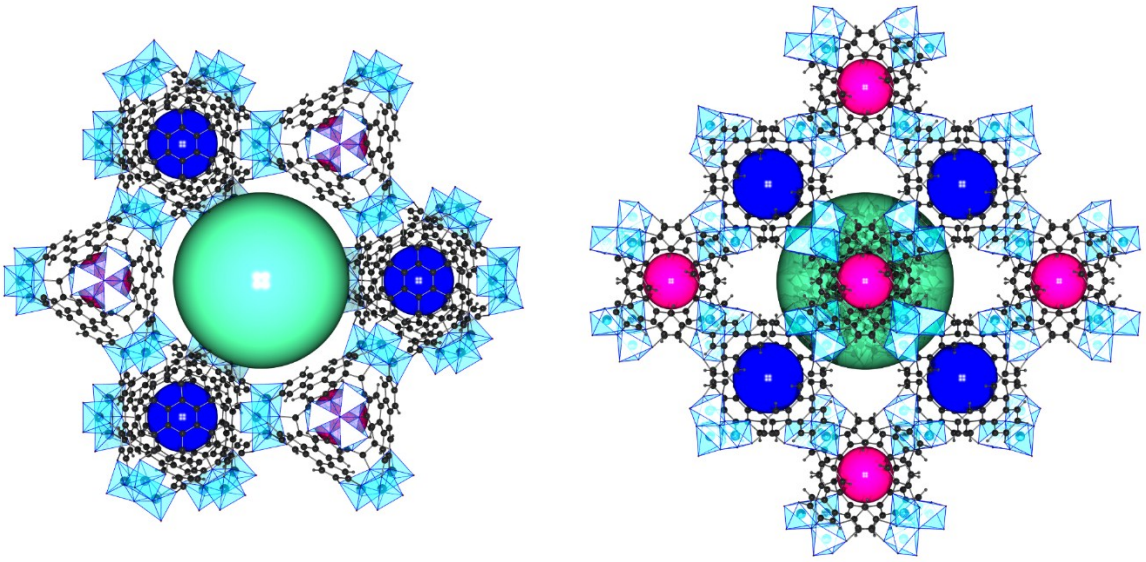

Fig. S4.3.7. Section of the Al-CAU-42 structure viewed along [111] (left) and [001] (right). Green spheres with a diameter of 16 Å represent the approximate pore space of the major tetrahedral pore of Al-CAU-42. AlO_6 polyhedra are represented in light blue. Aluminum: light blue, Carbon: black, Oxygen: red, Hydrogen: light grey.

4.4 Density Functional Theory (DFT) geometry optimization

The DFT geometry optimizations were performed using the Quickstep module[22] of the CP2K program[23,24] employing the Gaussian Plane Wave (GPW) formalism. The general gradient approximation (GGA) to the exchange-correlation functional according to Perdew-Burke-Ernzerhof (PBE)[25] was used in combination of Grimme's DFT-D3 semi-empirical dispersion corrections.[26,27] Triple-ζ plus valence polarized Gaussian-type basis sets (TZV2P-MOLOPT) were considered for all atoms, except for the Al metal centers, where double-ζ plus valence polarization functions (DZVP-MOLOPT) were employed.[28] The interaction between core electrons and valence shells of the atoms were described by the pseudopotentials derived by Goedecker, Teter, and Hutter (GTH).[29,30,31] The auxiliary plane wave basis sets were truncated at 400 Ry. In these calculations the atomic positions of the Al-CAU-42 structure models that have been determined by continuous rotation electron diffraction (cRED) were further relaxed retaining first the indexed cell parameters of the activated and purified phases. In order to maintain the same level of symmetry (space group *F23*) settings of the geometries, dimethylammonium (DMA^+) molecules were excluded from the DFT optimization. As such, instead of two DMA^+ ions per formula unit, a net charge of -2 (e) per IBU was considered, i.e., 2 additional electrons were added per IBU to make the system charge neutral. For both, purified and activated samples, it was found that the simulated PXRD pattern of the optimized structure shows a very good agreement with the experimentally observed patterns (see Fig. S4.4.1. and S4.4.2).

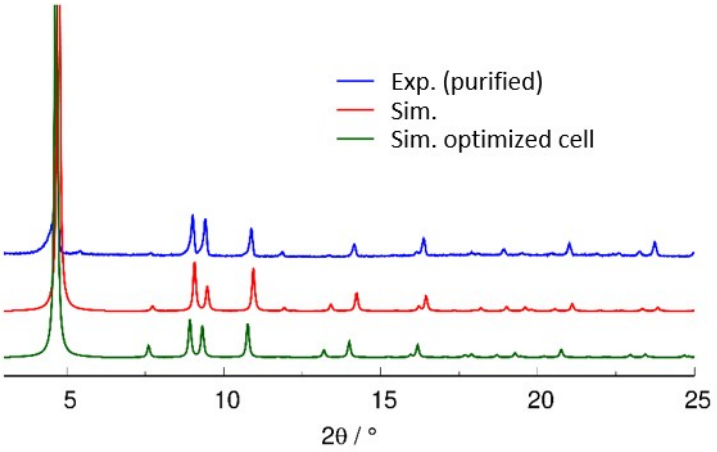

Fig. S4.4.1. Comparison of the PXRD patterns obtained from the experimental and DFT derived minimum energy structures with the cell parameters indexed from the powder data of purified sample and with the fully optimized cell parameters of Al-CAU-42.

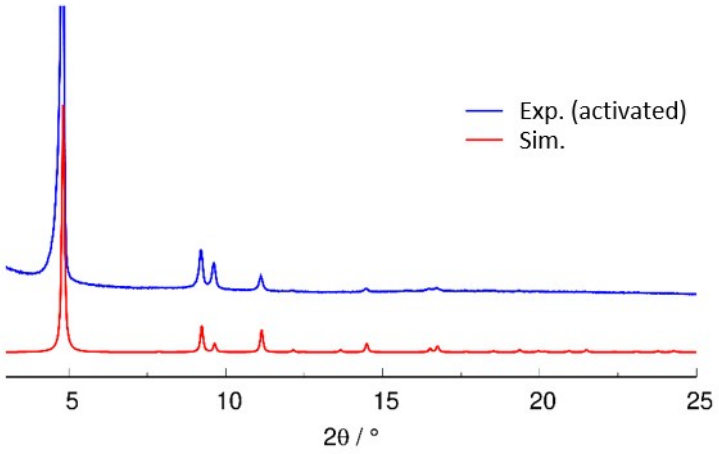

Fig. S4.4.2. Comparison of the PXRD patterns obtained from the experiment and DFT derived minimum energy structures of activated Al-CAU-42 sample.

Having the DFT minimum energy structures validated by the comparison of PXRD patterns, the required number of dimethylammonium ions was inserted in random positions of the free pore volume of the unit cell in accordance with the experimentally derived formula unit of the solid.
As a step further, the truly minimum energy conformer of the Al-CAU-42 solid was also checked, and for this, both the cell parameters and the atomic positions of the activated structure model were optimized simultaneously at the same DFT level. Thereby, a 3.5% isotropic expansion of the cell parameters and a constant shift of the peaks position compared to the purified sample as evidenced in the PXRD comparison drawn in Fig. S4.4.1 was noted.

Accessible surface area and Pore volume

The theoretical accessible surface areas (S_{acc}) of the geometric topology of the CAU-42(Al) MOFs were calculated using a simple Monte Carlo integration technique where the center of mass of the probe molecule with hard sphere is “rolled” over the framework surface.[32] In this method, a nitrogen sized (3.64 Å) probe molecule is randomly inserted around each framework atoms and the fraction of the probe molecules without overlapping with the other framework atoms is then used to calculate the accessible surface area. The Lennard-Jones size parameters of the framework atoms were taken from Universal Force Field (UFF).[33]
The free pore volume (V_{pore}) of the frameworks were further calculated using the same geometric method but with a probe molecule of 0 Å.[32]
The DMA^+ loaded model of purified Al-CAU-42 shows a N_2 accessible surface area of ~2100 m^2/g and a free pore volume of 1.07 cm^3/g. The activated sample shows very similar surface area but slightly smaller pore volume (1.00 cm^3/g) compared to the data simulated for the model of purified Al-CAU-42. These theoretically derived values are in relatively good agreement with the corresponding experimental data (for the activated solid: a_{BET} = 2170 m^2/g / V_{mic} = 0.81 cm^3/g) of Al-CAU-42. This further emphasizes the reliability of the DFT-model.

Pore size distribution (PSD)

The geometric methodology reported by Gelb and Gubbins[34] was used to calculate the pore size distributions (PSD) of the minimum DFT-energy structures, as depicted in Fig. S4.4.3. In these calculations, the van der Waals parameters of the framework atoms were adopted from Universal Force Field (UFF).[33]

Results

The resulting PSD shows that the largest tetrahedral cavity can accommodate a non-colliding sphere with a diameter of ~16 Å. The associated pore limiting diameter is ~15.5 Å. These tetrahedral cavities are surrounded by two variable sized super tetrahedral cages – formed by $HHTP^{6-/3\bullet-}$ trimeric units – with diameters of 4.8 and 5.5 Å. The pore size distribution of the model of activated Al-CAU-42 shows slightly narrower cavities compared to that of the purified compound (see Fig. S4.4.3) while one of the larger supertetrahedral cages widens by ~0.7 Å.

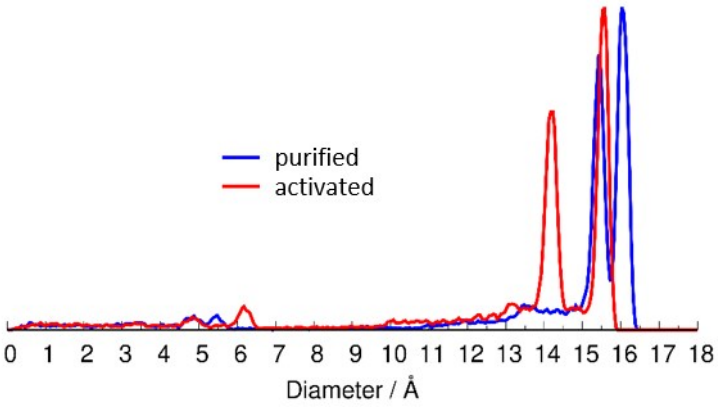

Fig. S4.4.3. Pore size distribution of purified and activated Al-CAU-42 frameworks calculated from the DFT optimized crystal structures.

The crystallographic information file (CIF) for DFT optimized purified Al-CAU-42 is given in the following. The CIF for the activated compound, as determined via cRED, can be obtained online from the CCDC (Cambridge Crystallographic Data Centre) with the identification number 1958798.

```
data_Al-CAU-42-asmade-dft-geometry-optimized_model
_chemical_name_systematic          H2[Al3O(HHTP)(HHTP*)]
_chemical_name_common              CAU-42(purified)
_chemical_formula_moiety           'C36 H14 Al3 O13'
_chemical_formula_sum              'C36 H14 Al3 O13'
_chemical_formula_weight           735.43
_chemical_compound_source          'newly synthesized compound'
_cell_length_a                     32.31010
_cell_length_b                     32.31010
_cell_length_c                     32.31010
_cell_angle_alpha                  90
_cell_angle_beta                   90
_cell_angle_gamma                  90
_cell_volume                       33729.891
_space_group_crystal_system        cubic
_space_group_IT_number             196
_space_group_name_H-M_alt          'F 2 3'
_space_group_name_Hall             'F 2 2 3'
_chemical_absolute_configuration ?
_diffrn_radiation_probe            x-ray
_diffrn_radiation_type             'Cu K\a1'
_diffrn_radiation_wavelength       1.5406

loop_
_symmetry_equiv_pos_as_xyz
  x,y,z
  -x,-y,z
  -x,y,-z
  x,-y,-z
  z,x,y
  z,-x,-y
  -z,-x,y
  -z,x,-y
  y,z,x
  -y,z,-x
  y,-z,-x
  -y,-z,x
  x,y+1/2,z+1/2
  -x,-y+1/2,z+1/2
  -x,y+1/2,-z+1/2
  x,-y+1/2,-z+1/2
  z,x+1/2,y+1/2
  z,-x+1/2,-y+1/2
```

-z,-x+1/2,y+1/2
-z,x+1/2,-y+1/2
y,z+1/2,x+1/2
-y,z+1/2,-x+1/2
y,-z+1/2,-x+1/2
-y,-z+1/2,x+1/2
x+1/2,y,z+1/2
-x+1/2,-y,z+1/2
-x+1/2,y,-z+1/2
x+1/2,-y,-z+1/2
z+1/2,x,y+1/2
z+1/2,-x,-y+1/2
-z+1/2,-x,y+1/2
-z+1/2,x,-y+1/2
y+1/2,z,x+1/2
-y+1/2,z,-x+1/2
y+1/2,-z,-x+1/2
-y+1/2,-z,x+1/2
x+1/2,y+1/2,z
-x+1/2,-y+1/2,z
-x+1/2,y+1/2,-z
x+1/2,-y+1/2,-z
z+1/2,x+1/2,y
z+1/2,-x+1/2,-y
-z+1/2,-x+1/2,y
-z+1/2,x+1/2,-y
y+1/2,z+1/2,x
-y+1/2,z+1/2,-x
y+1/2,-z+1/2,-x
-y+1/2,-z+1/2,x

loop_
_atom_site_label
_atom_site_type_symbol
_atom_site_fract_x
_atom_site_fract_y
_atom_site_fract_z
_atom_site_U_iso_or_equiv
_atom_site_adp_type
_atom_site_occupancy
Al1 Al 0.64502 0.65704 0.58934 0.00000 Uiso 1.00
C1 C 0.54266 0.57245 0.39425 0.00000 Uiso 1.00
C10 C 0.54199 0.60461 0.42434 0.00000 Uiso 1.00
C11 C 0.48273 0.63379 0.38960 0.00000 Uiso 1.00
C12 C 0.51172 0.63568 0.42046 0.00000 Uiso 1.00
C2 C 0.51129 0.57074 0.36372 0.00000 Uiso 1.00
C3 C 0.48041 0.60059 0.36095 0.00000 Uiso 1.00
C4 C 0.79495 0.66340 0.64370 0.00000 Uiso 1.00

```
C5    C    0.80220  0.63576  0.67721  0.00000  Uiso  1.00
C6    C    0.75680  0.66057  0.62240  0.00000  Uiso  1.00
C7    C    0.72789  0.63202  0.63438  0.00000  Uiso  1.00
C8    C    0.73551  0.60164  0.66550  0.00000  Uiso  1.00
C9    C    0.77306  0.60391  0.68602  0.00000  Uiso  1.00
O1    O    0.61530  0.61536  0.61532  0.00000  Uiso  1.00
O2    O    0.60052  0.66656  0.55037  0.00000  Uiso  1.00
O3    O    0.66486  0.61578  0.54677  0.00000  Uiso  1.00
O4    O    0.68870  0.63050  0.61955  0.00000  Uiso  1.00
O5    O    0.67383  0.70453  0.57491  0.00000  Uiso  1.00
H1    H    0.66776  0.58941  0.56367  0.00000  Uiso  1.00
H12   H    0.51062  0.66187  0.44160  0.00000  Uiso  1.00
H2    H    0.50980  0.54515  0.34190  0.00000  Uiso  1.00
H6    H    0.74745  0.68309  0.59924  0.00000  Uiso  1.00
H9    H    0.77826  0.58244  0.71145  0.00000  Uiso  1.00

loop_
_geom_bond_atom_site_label_1
_geom_bond_atom_site_label_2
_geom_bond_distance
_geom_bond_site_symmetry_1
_geom_bond_site_symmetry_2
_geom_bond_publ_flag
 Al1  O1     1.8552 .  .  yes
 Al1  O2     1.9358 .  .  yes
 Al1  O3     2.0199 .  .  yes
 Al1  O4     1.9183 .  .  yes
 Al1  O5     1.8543 .  .  yes
 O4   C7     1.3548 .  .  yes
 C1   C2     1.4154 .  .  no
 C1   C10    1.4232 .  .  no
 C2   C3     1.3906 .  .  no
 C3   C11    1.4189 .  .  no
 C4   C5     1.4229 .  .  no
 C4   C6     1.4147 .  .  no
 C5   C9     1.4235 .  .  no
 C6   C7     1.3687 .  .  no
 C7   C8     1.4266 .  .  no
 C8   C9     1.3845 .  .  no
 C10  C12    1.4071 .  .  no
 C11  C12    1.3694 .  .  no
 C2   H2     1.0900 .  .  no
 C6   H6     1.0900 .  .  no
 C9   H9     1.0900 .  .  no
 C12  H12    1.0900 .  .  no
```

5. EPR spectroscopy

The EPR spectra measured at room temperature using a modulation amplitude of 4G and microwave power of 2.0 mW are shown in Figure S5.1.

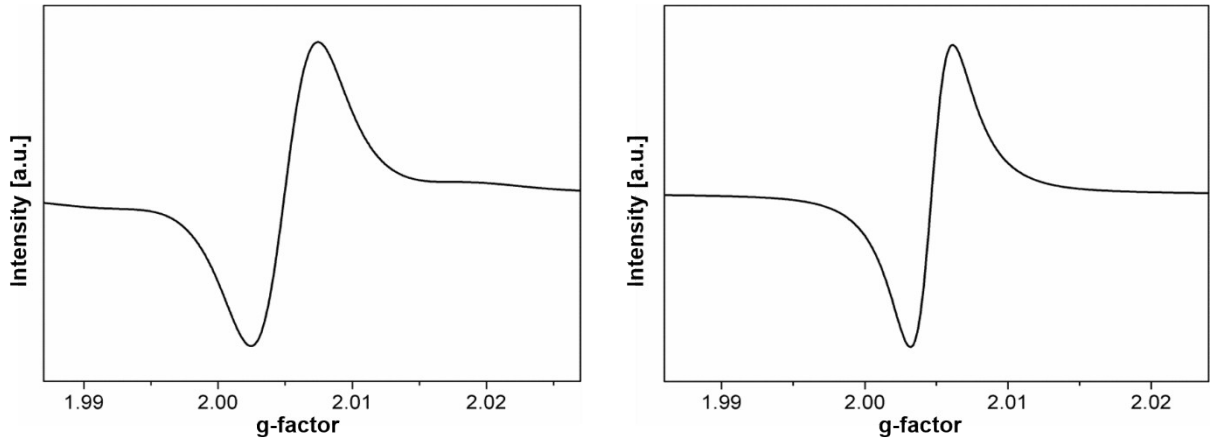

Fig. S5.1. g-Transformation of the EPR spectra of Al-CAU-42 (left) and Ga-CAU-42 (right).

The EPR spectra confirm the presence of unpaired electrons in the two title compounds. The symmetric signal yield in both measurements a g-value of approximately 2.005, which is characteristic for the presence of monoradical ions. Thus, the linker is partially reduced during the synthesis and forms the monoradical ion $HHTP^{\bullet 3-}$ (Fig. S.5.2).[35,36]

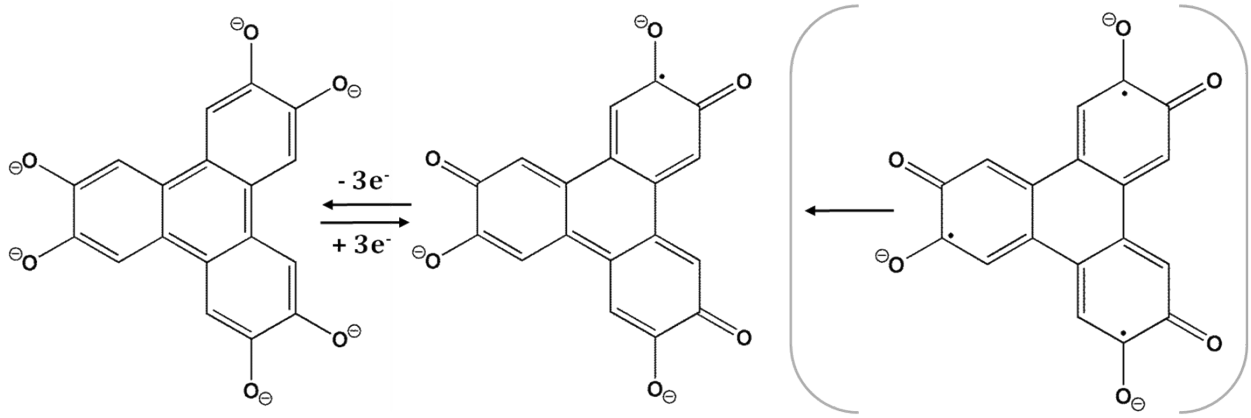

Fig. S5.2. Linker molecule in the CCC (left, $HHTP^{6-}$) and the SSS (right, $HHTP^{\cdots 3-}$) form (see Fig. S1.1). Spin pairing of two electrons leads to the formation of the monoradical SSS form (middle, $HHTP^{\bullet 3-}$).

6. Sorption measurements

The samples were thermally activated at 170 °C for 12h under reduced pressure. Nitrogen sorption measurements at 77 K were carried out to determine the porosity of the materials. To determine the permanent porosity of the samples, measurements were cycled three times and in between the measurements the samples were kept under vacuum.

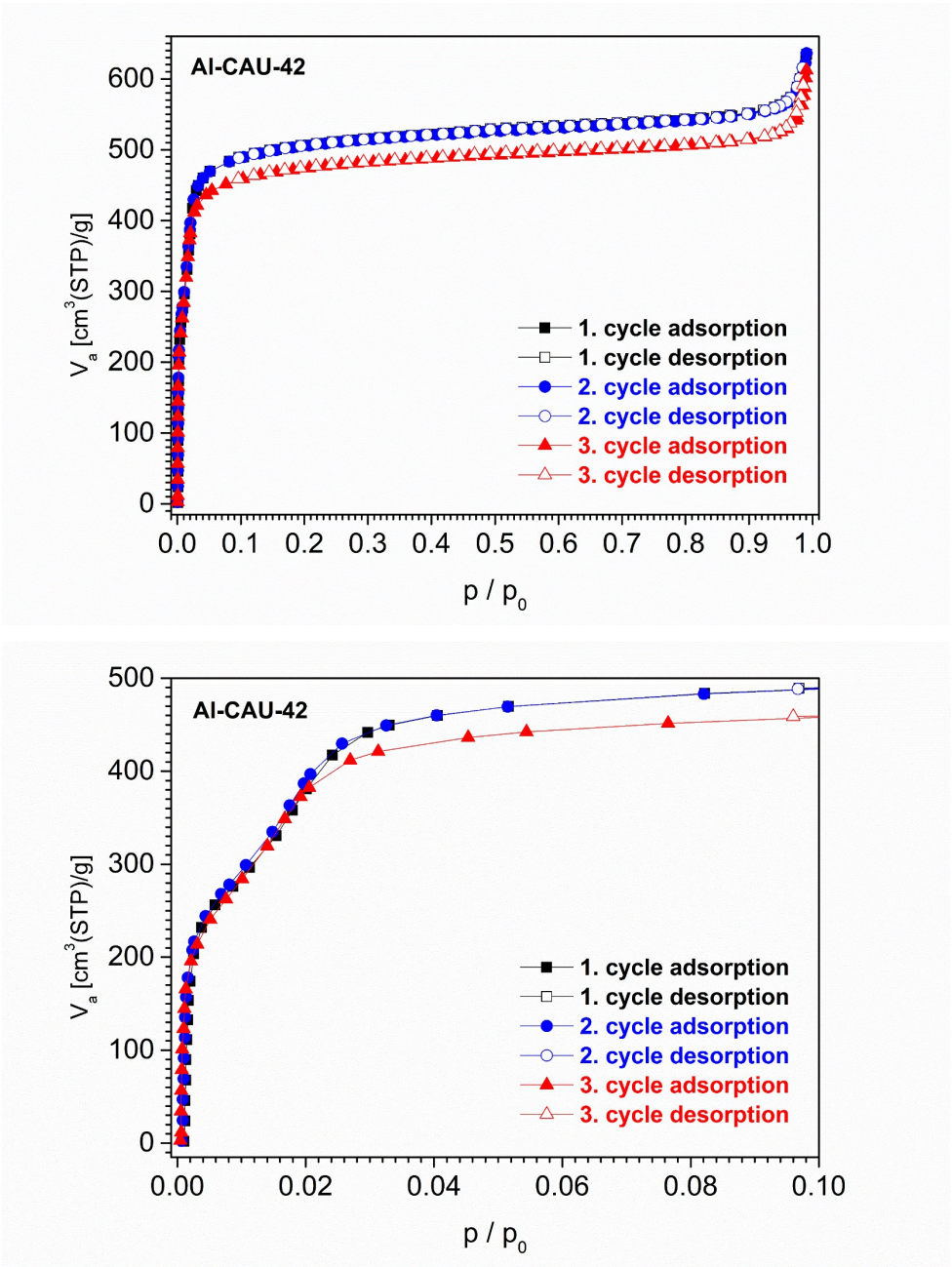

Fig. S6.1. Nitrogen adsorption isotherms of multiple adsorption/desorption cycles for Al-CAU-42 (top) with magnification of the low pressure range (bottom).

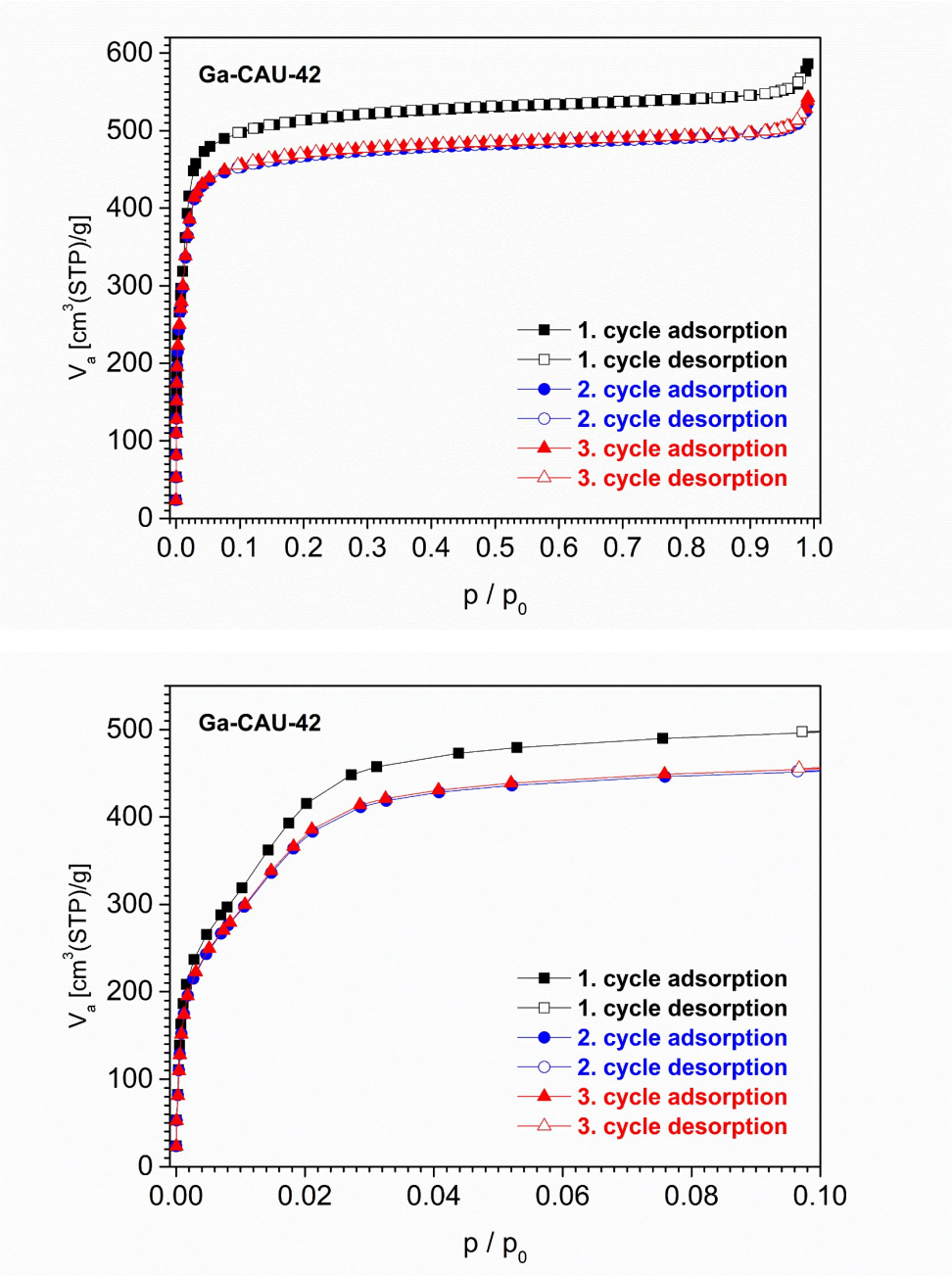

Fig. S6.2. Nitrogen adsorption isotherms of multiple adsorption/desorption cycles for Ga-CAU-42 (top) with magnification of the low pressure range (bottom).

Small changes between the measurements are clearly visible. For both compounds the first measurements results in the highest N_2 uptake. Although for Al- and Ga-CAU-42 a decrease of N_2 uptake in the third and second cycle, respectively, is observed, the high permanent porosity is demonstrated. The samples exhibit Type I isotherms with a step at $p/p_0 \approx 0.001$ which is probably due to the large 3D pore system with a diameter of 16 Å.

Evaluation of the isotherms by the BET methods using the approach described by Roquerol[37] resulted in specific surface areas and micropore volumes as high as $a_{BET} = 2170\ m^2g^{-1}$ / $V_{mic} = 0.81\ cm^3g^{-1}$ for Al-CAU-42 and $a_{BET} = 2020\ m^2g^{-1}$ / $V_{mic} = 0.82\ cm^3g^{-1}$ for Ga-CAU-42 (Tab S6.1). The micropore volume was determined at $p/p_0 = 0.5$ and is smaller than the theoretical value ($V_{mic,\ theo} = 1.00\ cm^3g^{-1}$). This deviation could be caused by sample decomposition to a small extent during thermal activation. It is likely that the surface area is slightly overestimated by the BET method, since the nitrogen uptake at low p/p_0 is not perfectly

linear. Nevertheless, the porosities exceed the ones for other MOFs obtained with the H_6HHTP linker molecule by far. For Co-CAT-1[38] and V-CAT-5[39] values of 490 and 725 m^2/g were reported.

Tab. S6.1 Specific surface areas and micropore volumes of Al- and Ga-CAU-42 calculated from each of the three isotherms.

Cycle	Al-CAU-42		Ga-CAU-42	
	a_{BET} / cm^2g^{-1}	V_{micro} / cm^3g^{-1}	a_{BET} / cm^2g^{-1}	V_{micro} / cm^3g^{-1}
1	2170	0.81	2020	0.82
2	2150	0.81	1860	0.75
3	1940	0.76	1840	0.75

In addition, CO_2 adsorption isotherms were recorded at 298 K (Fig. 6.3) and uptakes of 5.5 and 7.0 wt% at 100 kPa are observed for Al- and Ga-CAU-42 respectively.

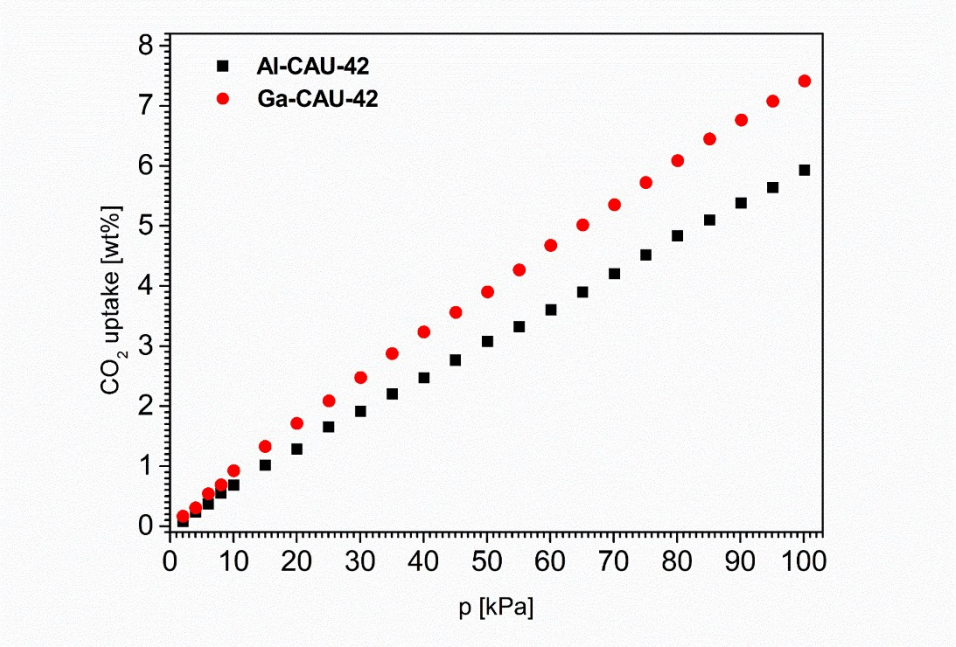

Fig. S6.3. CO_2 adsorption isotherms of Al-CAU-42 (black) and Ga-CAU-42 (red), recorded at 298 K.

To confirm the crystallinity of both compounds after the N_2 sorption measurements PXRD patterns of both compounds were recorded (Fig. S7.4 and S7.5). The crystallinity of both compounds is reduced after the adsorption cycles.

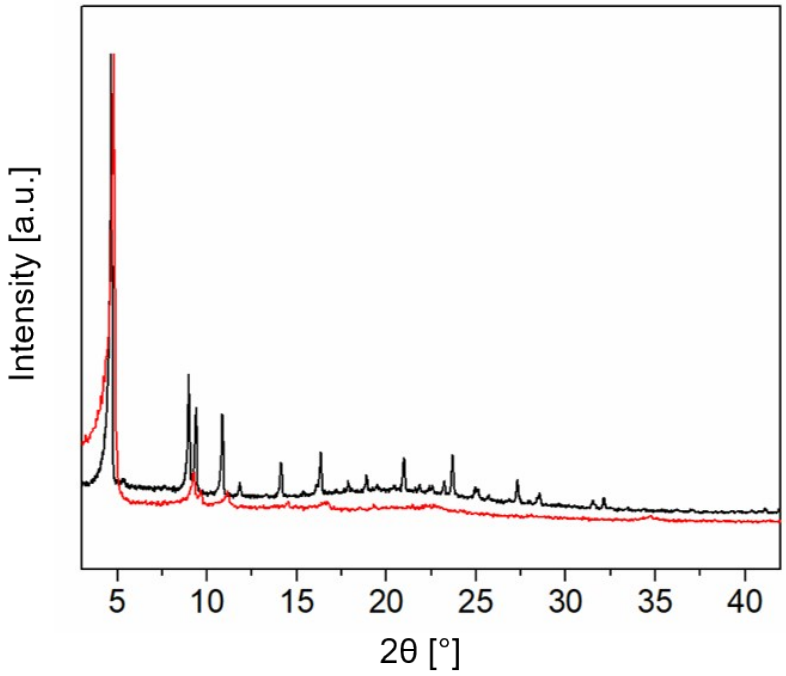

Fig. S6.4. PXRD pattern of Al-CAU-42 before (black) and after (red) the sorption measurement.

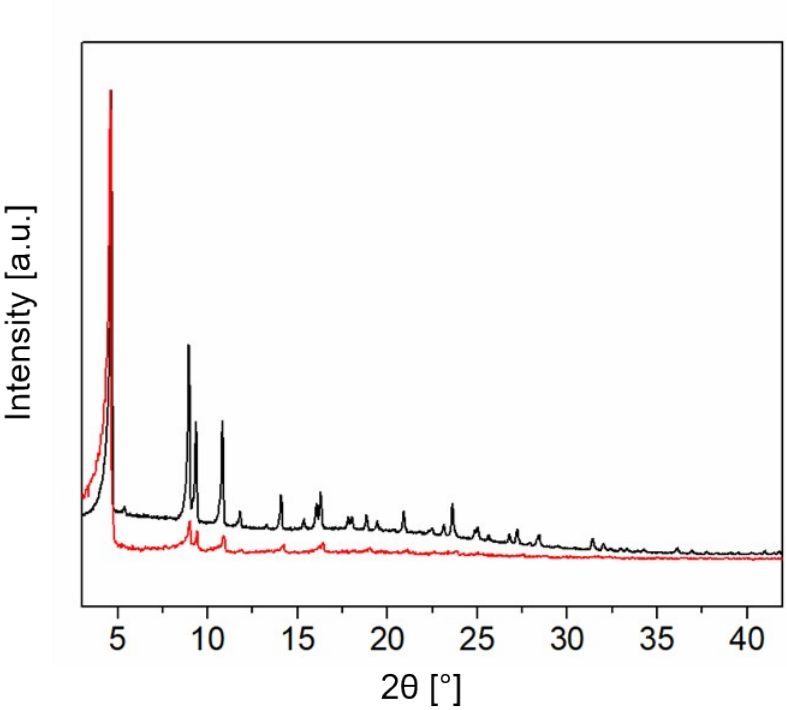

Fig. S6.5. PXRD pattern of (Ga-CAU-42) before (black) and after (red) the sorption measurement.

7. Thermal and elemental analysis

To determine the thermal stability thermogravimetric (TG) and variable-temperature PXRD (VT-PXRD) measurements were carried out. The TG curves were recorded under a flow of air (75 cm^3 min^{-1}) using a heating rate of 2 °C min^{-1} (Fig. S7.1, Fig. S7.2, Tab. S7.1, Tab. S7.2). The samples were also analyzed by elemental analysis (Tab. S7.3).

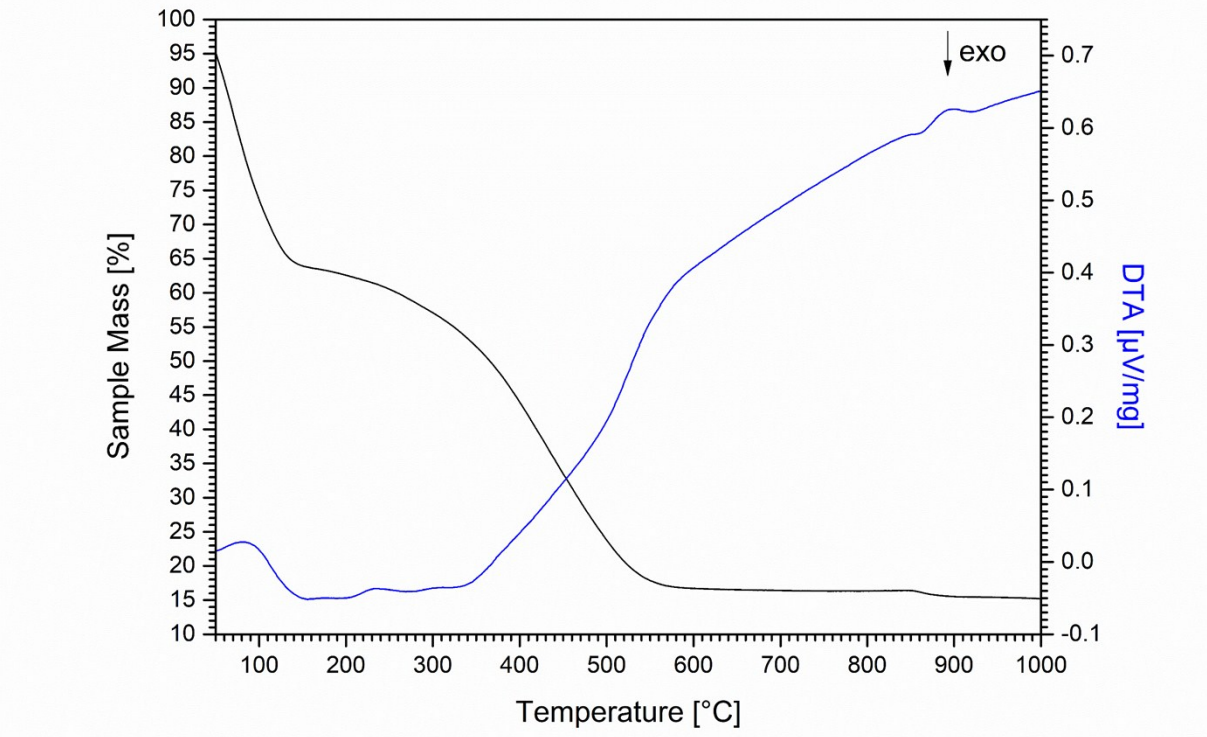

Fig. S7.1. TG/DTA curve of $((CH_3)_2NH_2)_2[Al_3O(HHTP)(HHTP^{\bullet})]\cdot 0.5DMF\cdot 18H_2O$ (Al-CAU-42).

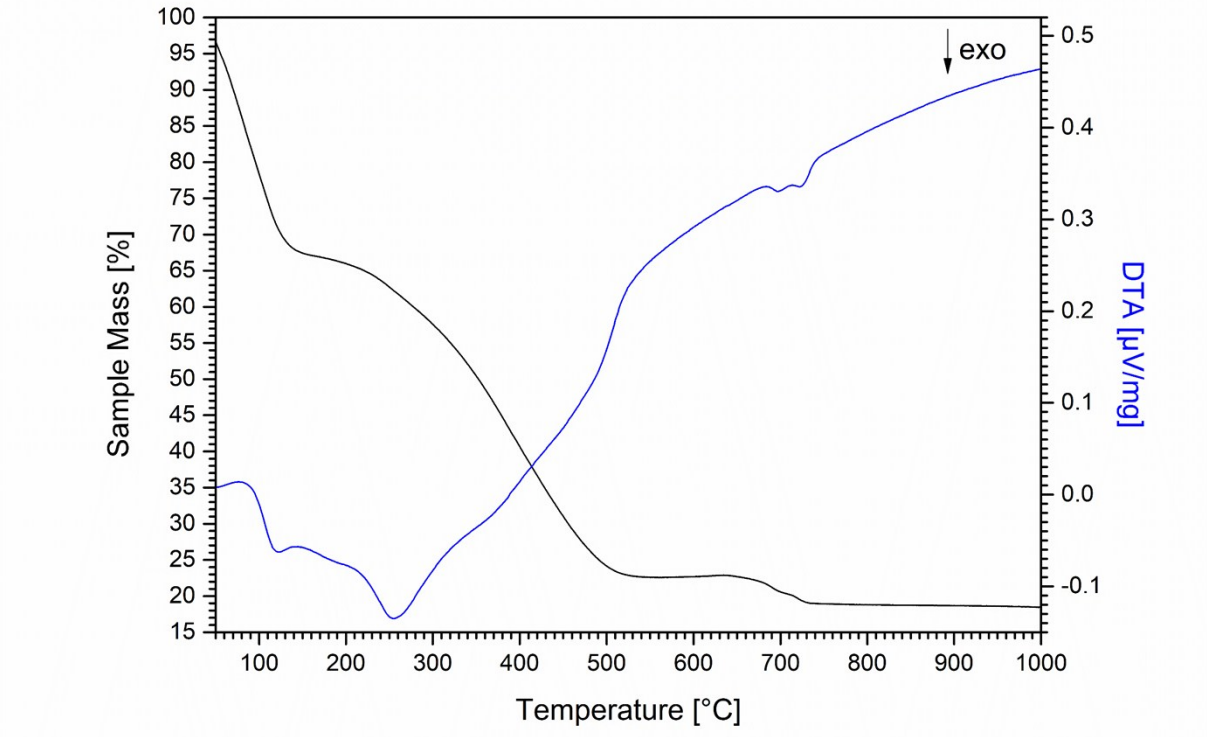

Fig. S7.2. TG/DTA curve of $((CH_3)_2NH_2)_2[Ga_3O(HHTP)(HHTP^{\bullet})]\cdot 14.5H_2O$ (Ga-CAU-42).

Both TG curves exhibit three discrete weight losses between 50 and 1000 °C. The first weight loss for both compounds can be attributed to the release of solvent molecules (water and small amounts of DMF) and dimethylammonium ions (as dimethylamine) and is completed at ~160 °C. The remaining two weight losses represent the decomposition of the framework. The second weight loss can be attributed to the combustion of the linker molecules while the third weight loss might be most likely explained by the release of residual CO_2 originating from carbon-containing combustion intermediates. According to the PXRD measurements which were carried out after TG analysis an X-ray amorphous product is formed for Al-CAU-42. It has probably the composition Al_2O_3. For Ga-CAU-42 Ga_2O_3 is formed (Fig. S7.3). The TG results compare well with the results of the CHNS analyses (Tab. S7.3.)

Tab. S7.1. Results of the TG analyses of Al-CAU-42 with the composition $((CH_3)_2NH_2)_2[Al_3O(HHTP)(HHTP^{\bullet})]\cdot 0.5DMF\cdot 18H_2O$.

Mass loss	Temp. range [°C]	Experimental [%]	Calculated [%]
H_2O/DMF evaporation	25 - 160	36.5	36.5
MOF decomposition	160 - 900	48.3	50.4
Residue (Al_2O_3)	>900	15.2	13.1

Tab. S7.2. Results of the TG analyses of Ga-CAU-42 with the composition $((CH_3)_2NH_2)_2[Ga_3O(HHTP)(HHTP^{\bullet})]\cdot 14.5H_2O$.

Mass loss	Temp. range [°C]	Experimental [%]	Calculated [%]
H_2O evaporation	25 - 160	29.6	28.9
MOF decomposition	160 - 750	48.5	48.0
Residue (Ga_2O_3)	>750	21.9	23.1

Tab. S7.3. Elemental analyses of $((CH_3)_2NH_2)_2[Al_3O(HHTP)(HHTP^{\bullet})]\cdot 0.5DMF\cdot 18H_2O$ (Al-CAU-42) and $((CH_3)_2NH_2)_2[Ga_3O(HHTP)(HHTP^{\bullet})]\cdot 14.5H_2O$ (Ga-CAU-42).

Element	Al-CAU-42	Ga-CAU-42
Carbon *experimental* [%]	41.9	36.6
Carbon *calculated* [%]	41.8	39.0
Hydrogen *experimental* [%]	4.4	3.8
Hydrogen *calculated* [%]	6.2	5.2
Nitrogen *experimental* [%]	3.3	2.7
Nitrogen *calculated* [%]	2.9	2.3

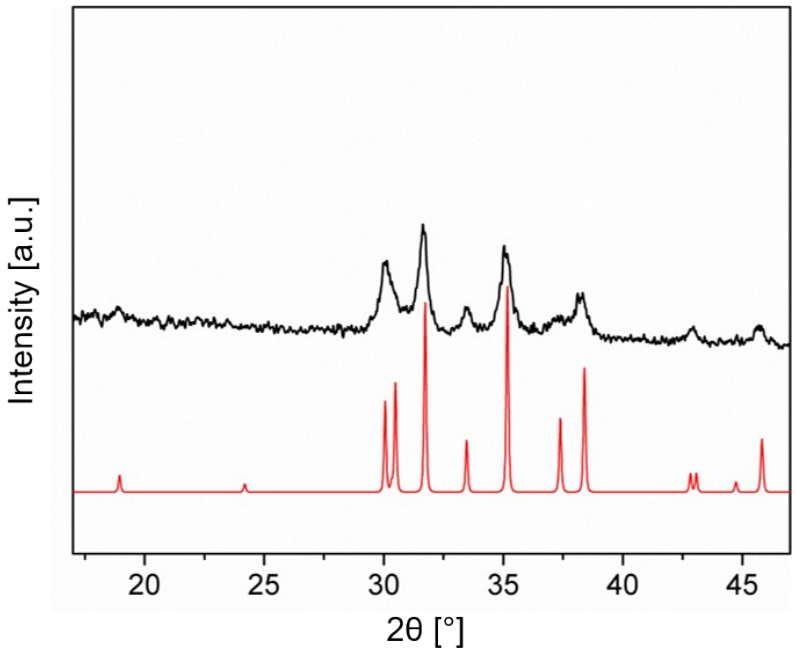

Fig. S7.3. Measured PXRD pattern of the thermogravimetric decomposition product of Ga-CAU-42 (black) and calculated PXRD pattern of crystalline β-Ga_2O_3 (red).[40]

8. Variable-temperature PXRD measurements

Temperature dependent PXRD measurements were carried out between 30 and 480 °C in steps of 30 °C after temperature equilibration for 10 min. A heating rate of 10 °C min^{-1} was employed. The results are shown in Figure S8.1 and S8.2 for Al- and Ga-CAU-42, respectively.

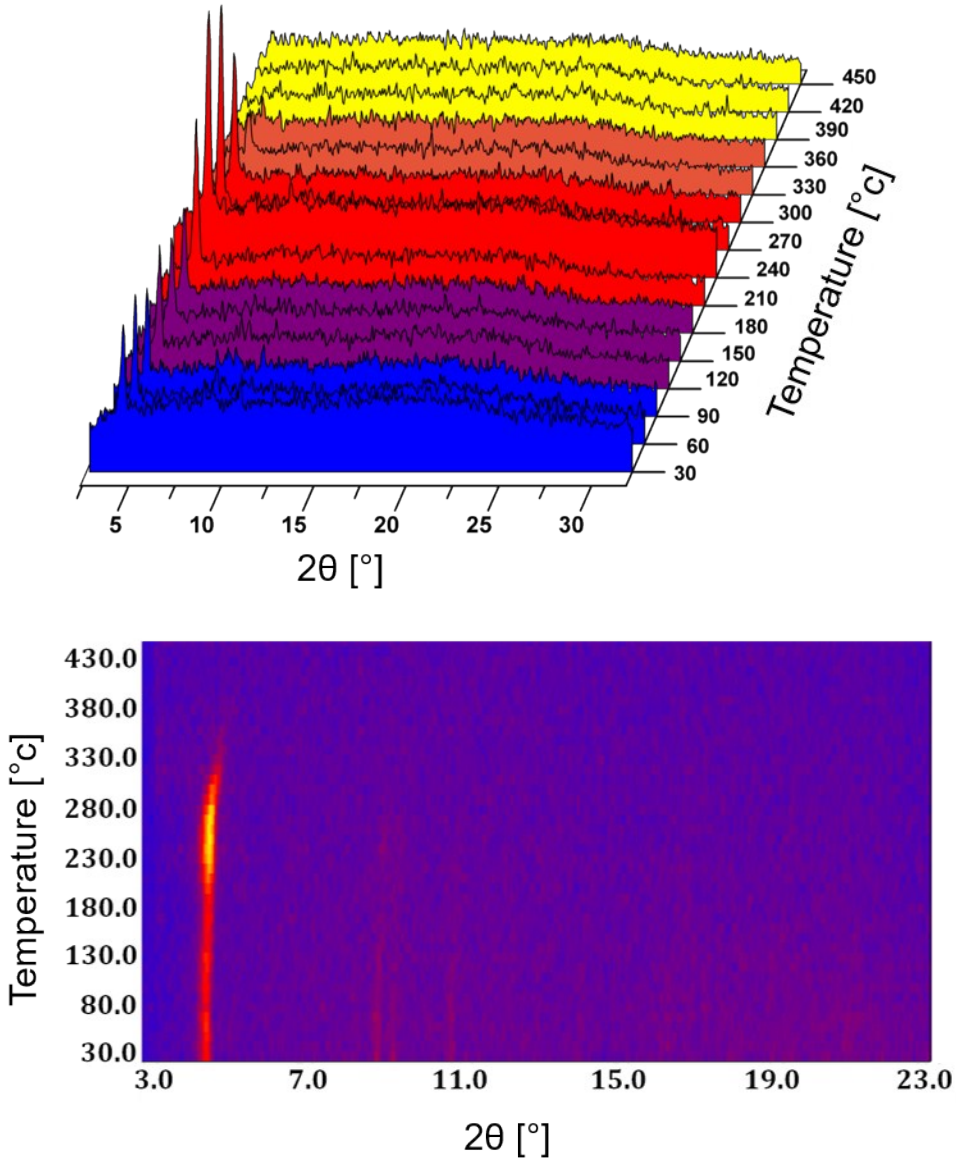

Fig. S8.1. 3D (top) and 2D (bottom) representation of the results of the VT-PXRD measurements of $((CH_3)_2NH_2)_2[Al_3O(HHTP)(HHTP^{\bullet})]\cdot 0.5DMF\cdot 18H_2O$.

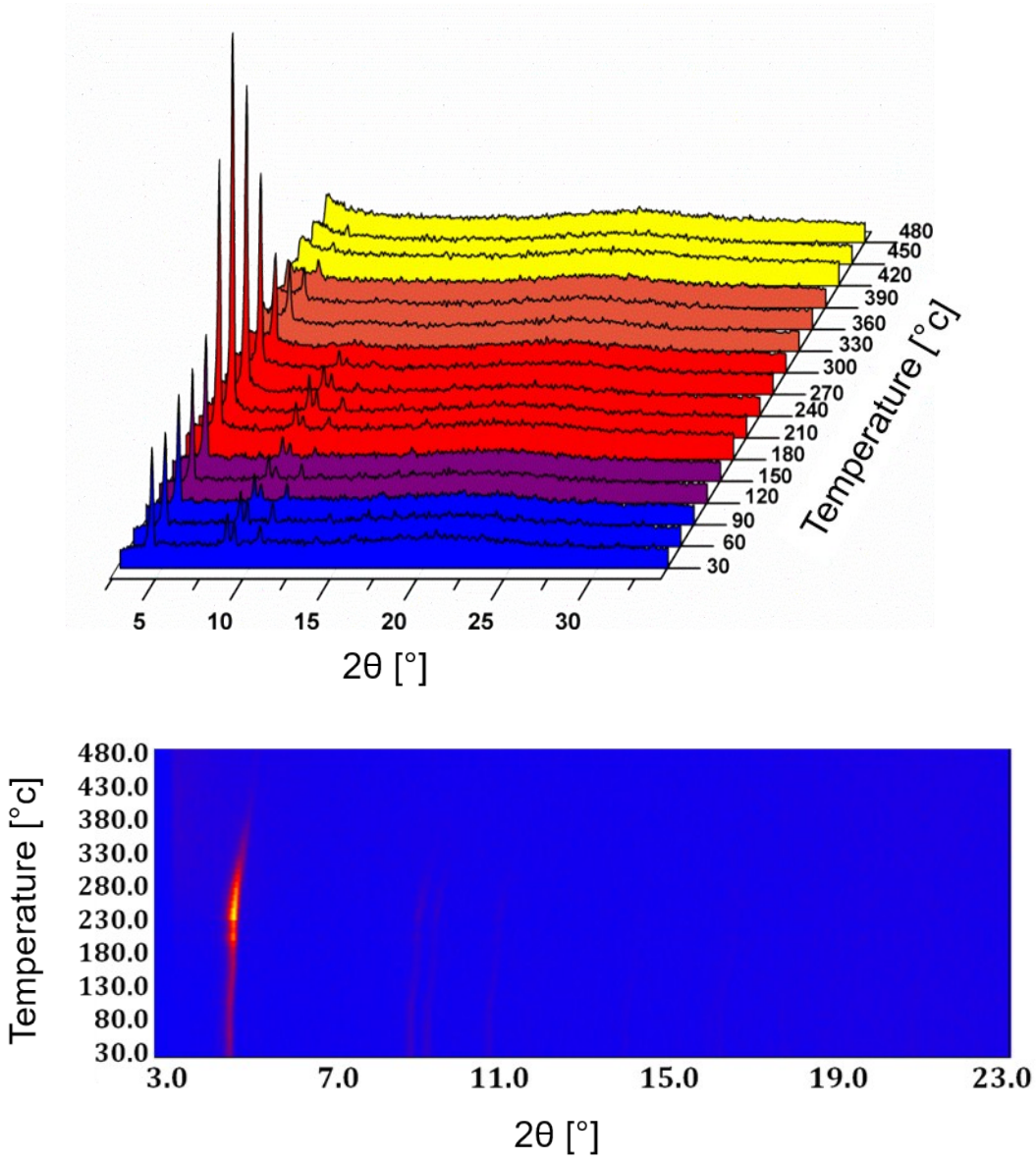

Fig. S8.2. 3D (top) and 2D (bottom) representation of the results of the VT-PXRD measurements of $((CH_3)_2NH_2)_2[Ga_3O(HHTP)(HHTP^{\bullet})]\cdot 14.5H_2O$.

9. IR spectroscopy

Al- and Ga-CAU-42 were also characterized by IR spectroscopy (Fig. S9.1). Assignments for the most important IR bands are given in Tab. S9.1.

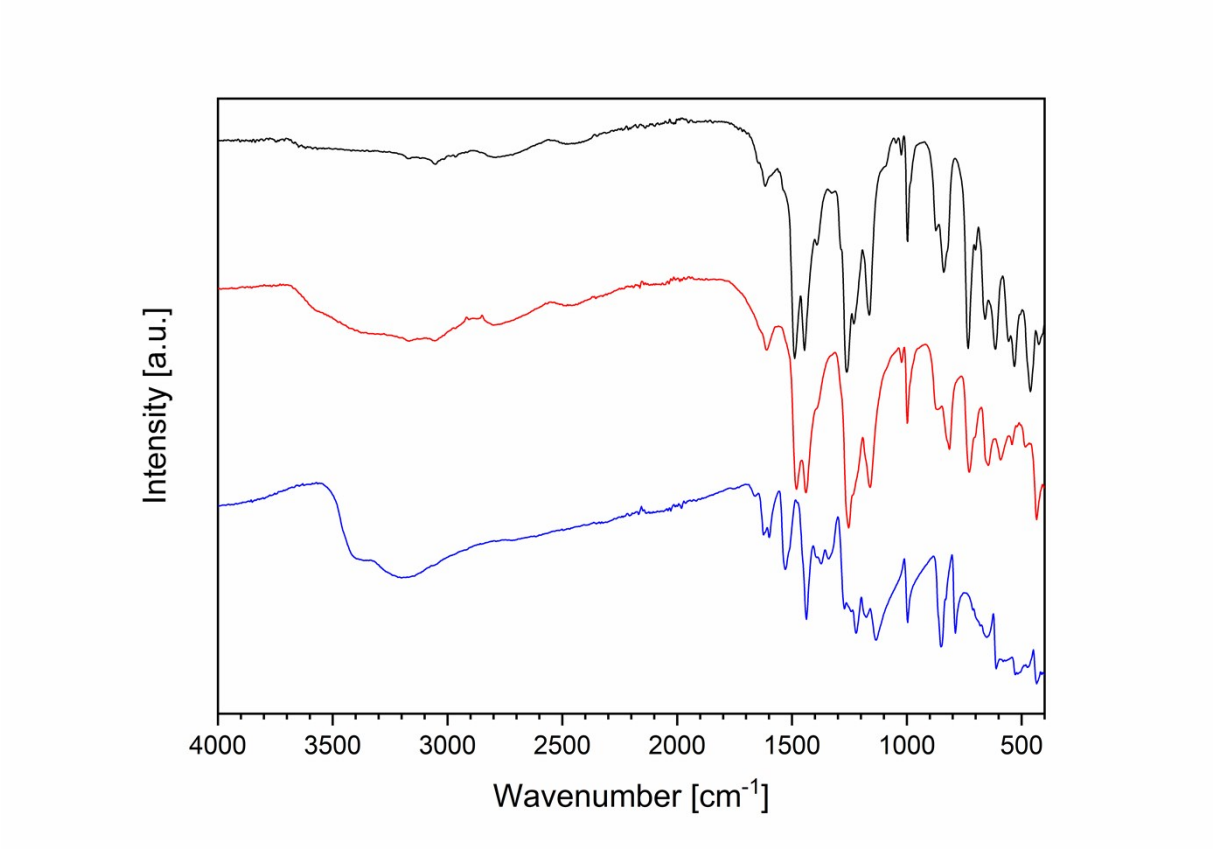

Fig. S9.1. Infrared spectra of Al-CAU-42 (black), Ga-CAU-42 (red) and H_6HHTP (blue).

Tab. S9.1. Assignment[41] of the bands observed in the IR-spectra of Al-CAU-42 and Ga-CAU-42.

Al-CAU-42 $\tilde{\nu}$ [cm^{-1}]	**Ga-CAU-42** $\tilde{\nu}$ [cm^{-1}]	**Assignment**
3670 - 2890	3670 - 2890	*v* (O-H), involved in hydrogen bonds, water
3055	3055	*v* (C-H), aromatic protons, HHTP
2786	2786	sym. *v* (C-H), CH_3, dimethylammonium ion
2455	2455	*v* (N-H), dimethylammonium ion
1647	1647	*v* (C=O) polycyclic *ortho*-quinones
1618	1609	*δ* (N-H), dimethylammonium & *v* (C=C), HHTP
1479, 1442, 1391	1479, 1442, 1391	*v* (C=C), HHTP
1161, 998	1161, 998	*v* (C-O), HHTP
838, 729, 658	817, 729, 646	*δ* (C-H), HHTP

10. Solid-state NMR spectroscopy (ss-NMR)

Solid-state NMR experiments were carried out with Al-CAU-42 in order to investigate the chemical environment of the Al^{3+} ions of the IBU. To avoid sample degradation as far as possible, Al-CAU-42 was freshly prepared and thoroughly washed with DMF. After evaporation of the DMF over three days in air at RT ^{1}H MAS, ^{1}H-^{27}Al-TRAPDOR and ^{27}Al NMR spectra were directly collected (sample name: Al-CAU-42 (DMF)). Due to an overlap of the methyl proton signals of DMF and the postulated dimethylammonium ions (DMA^{+}) another sample from the same batch was prepared. This time it was additionally washed with ethanol (1x) and dichloromethane (10x) to remove all residual DMF molecules. After evaporation of the dichloromethane over two weeks in air at RT, again a ^{1}H MAS NMR and ^{1}H-^{27}Al-TRAPDOR spectrum was recorded in order to verify the presence of DMA^{+} ions (sample name: Al-CAU-42 (DCM)). The results of the different measurements are shown in Fig. S10.1.

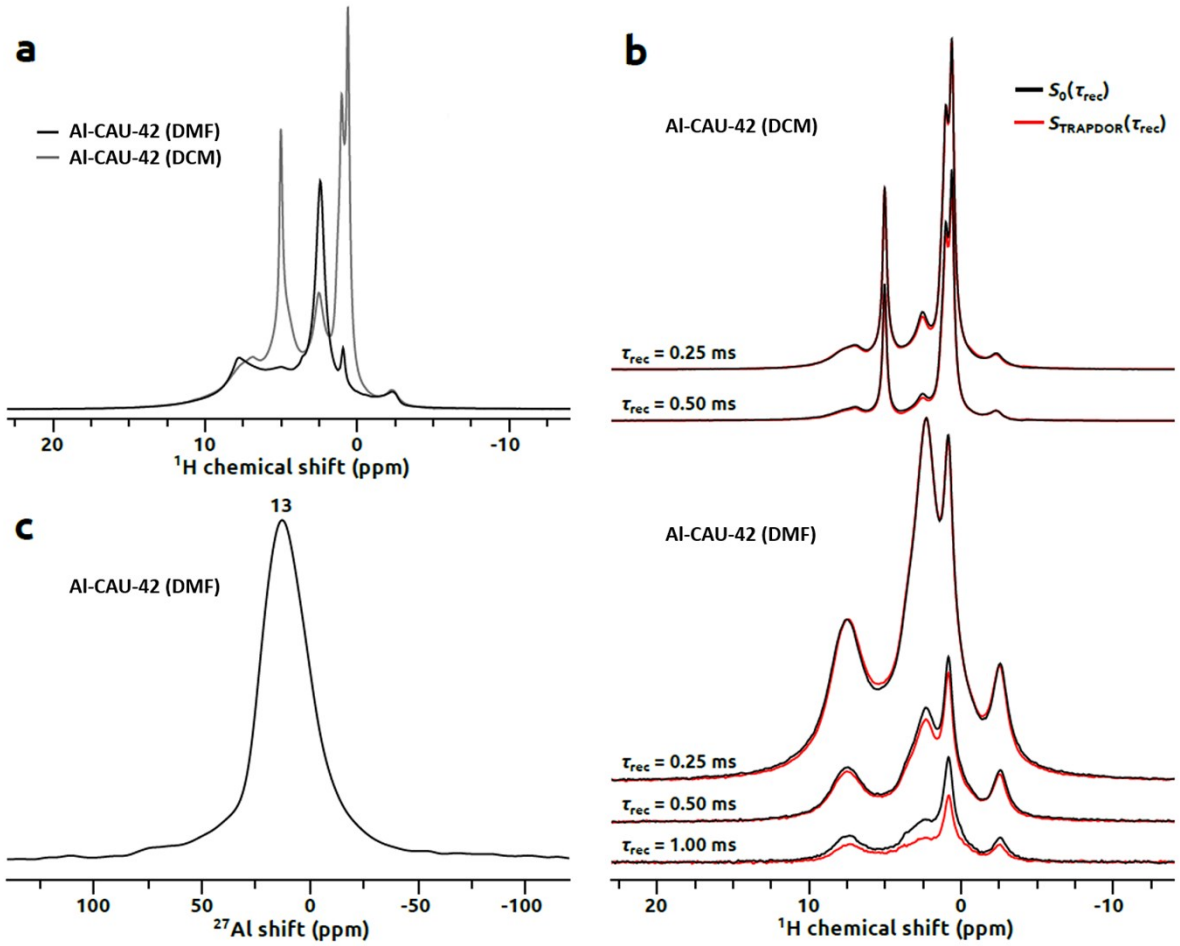

Fig. S10.1. ^{1}H MAS NMR (**a**), ^{1}H-^{27}Al-TRAPDOR (**b**) and ^{27}Al NMR spectra (**c**) of Al-CAU-42 (DMF) and Al-CAU-42 (DCM).

The ^{1}H MAS NMR spectrum of Al-CAU-42 (DMF) shows a primary signal at 2.4 ppm which corresponds to -CH_3 groups from a mixture of DMF and DMA^{+} ions. The -CHO protons of DMF are expected to contribute to the signal at ~8 ppm. In contrast, the ^{1}H MAS NMR spectrum of Al-CAU-42 (DCM) shows a less intense signal at 2.5 ppm. It could only be observed due to the prior solvent exchange described above and is therefore very likely to correspond to DMA^{+} ions. The signal at 5 ppm originates from dichloromethane and the signal at 1 ppm is

characteristic for -OH groups terminating the IBU. The presence of terminating -OH groups at the IBU shows that the exposure of the material to air already led to a partial degradation. The signal at -2.5 ppm exhibits a negative shift, which is unusual. It probably arises from an interaction of a proton with the paramagnetic linker molecule.

Dephasing of the proton signal at 2.4 ppm in the ^{1}H-^{27}Al-TRAPDOR spectrum of Al-CAU-42 (DMF) collected with recoupling time of 0.5 ms indicates that these protons are in closer spatial proximity to Al^{3+} than the others. At 1.00 ms an approximately uniform dephasing of the remaining signals is observed, which means that at this recoupling time protons from linker moieties are recoupled. The preferential dephasing of the signal at 2.5 ppm is also observed in the ^{1}H-^{27}Al-TRAPDOR spectrum of Al-CAU-42 (DCM). Therefore, both DMF and the DMA^{+} ions are close to the IBU. The proximity of the DMA^{+} ions to the IBU is reasonable since they establish charge compensation.

The ^{27}Al NMR spectrum of Al-CAU-42 (DMF) shows a broadened signal. The broadening can be related to disorder within the environment of Al^{3+} in the form of slight bond distance and angle deviations, which results in chemical shifts and quadrupolar couplings distribution. This is expected since a part of the linker molecules is present in its monoradical state.

References

[1] A. A. Coelho, *J. Appl. Cryst.* **2018**, *51*, 210-218.

[2] A. K. Rappe, C. J. Casewit, K. S. Colwell, W. A. GoddardIII, W. M. Skiff, *J. Am. Chem. Soc.* **1992**, *114*, 10024-10035.

[3] Accelrys Materials Studio Version 5.0, San Diego, CA, **2009**.

[4] J. Rouquerol, P. Llewellyn, F. Rouquerol, *Stud. Surf. Sci. Catal.* **2007**, *160*, 49-56.

[5] A. L. Spek, *Acta. Cryst.* **2009**, *D65*, 148-155.

[6] Amsterdam Scientific Instruments, "Timepix QTPX-262k: A hybrid pixel detector for X-ray applications," can be found under http://www.amscins.com/site/wp-content/uploads/2014/06/A5_QTPX_specs_Xray_digital.pdf, **2014**.

[7] T. L. Hwang, P. C. M. van Zijl, M. Garwood, *J. Magn. Reson.* **1998**, *133*, 200-203.

[8] G. Kervern, G. Pintacuda, L. Emsley, *Chem. Phys. Lett.* **2007**, *435*, 157-162.

[9] A. J. Pell, G. Pintacuda, *Prog. Nucl. Mag. Res. Sp.* **2015**, *84-85*, 33-72.

[10] C. P. Grey, W. S. Veeman, *Chem. Phys. Lett.* **1992**, *192*, 379-385.

[11] N. Stock *Microporous Mesoporous Mater.* **2010**, *129*, 287-295; N. Stock and S. Biswas, *Chem. Rev.*, 2012, **112**, 933-969.

[12] G.S. Pawley, *Appl. Crystallogr.* **1981**, *14*, 357.

[13] A. Coelho, *TOPAS Academic*, Coelho Software, **2016**.

[14] A.C. Sudik, A.P. Côté, A.G. Wong-Foy, M. O'Keeffe, O.M. Yaghi, *Angew. Chem. Int. Ed.* **2006**, *45*, 2528.

[15] D. Feng, K. Wang, J. Su, T.-F. Liu, J. Park, Z. Wei, M. Bosch, A. Yakovenko, X. Zou, H.C. Zhou, *Angew. Chem. Int. Ed.* **2015**, *54*, 149.

[16] R. W. G. Wyckoff, *Z. Kristallogr. - Cryst. Mater.* **1925**, *62*, 189-200.

[17] G. Winter, D. G. Waterman, J. M. Parkhurst, A. S. Brewster, R. J. Gildea, M. Gerstel, L. Fuentes-Montero, M. Vollmar, T. Michels-Clark, I. D. Young, et al., *Acta Crystallogr. Sect. Struct. Biol.* **2018**, *74*, 85-97.

[18] P. R. Evans, G. N. Murshudov, *Acta Crystallogr. D Biol. Crystallogr.* **2013**, *69*, 1204-1214.

[19] G. M. Sheldrick, Acta Crystallogr. *Sect. Found. Adv.* **2015**, *71*, 3-8.

[20] G. M. Sheldrick, Acta Crystallogr. *Sect. C Struct. Chem.* **2015**, *71*, 3-8.

[21] C. B. Hübschle, G. M. Sheldrick, B. Dittrich, *J. Appl. Crystallogr.* **2011**, *44*, 1281-1284.

[22] J. VandeVondele, M. Krack, F. Mohamed, M. Parrinello, T. Chassaing and J. Hutter, *Comput. Phys. Commun.* **2005**, *167*, 103-128.

[23] J. Hutter, M. Iannuzzi, F. Schiffmann and J. VandeVondele, *Wiley Interdiscip. Rev. Comput. Mol. Sci.* **2014**, *4*, 15-25.

[24] The CP2K developers group, http://www.cp2k.org, (accessed 10 February 2019).

[25] J. P. Perdew, K. Burke and M. Ernzerhof, *Phys. Rev. Lett.* **1996**, *77*, 3865-3868.

[26] S. Grimme, J. Antony, S. Ehrlich and H. Krieg, *J. Chem. Phys.* **2010**, *132*, 154104.

[27] S. Grimme, *J. Comput. Chem.* **2004**, *25*, 1463-73.

[28] J. VandeVondele and J. Hutter, *J. Chem. Phys.* **2007**, *127*, 114105.

[29] S. Goedecker, M. Teter and J. Hutter, *Phys. Rev. B* **1996**, *54*, 1703-1710.

[30] M. Krack, *Theor. Chem. Acc.* **2005**, *114*, 145-152.

[31] C. Hartwigsen, S. Goedecker and J. Hutter, *Phys. Rev. B* **1998**, *58*, 3641-3662.

[32] T. Duren, F. Millange, G. Ferey, K. S. Walton and R. Q. Snurr, *J. Phys. Chem. C* **2007**, *111*, 15350-15356

[33] A. K. Rappe, C. J. Casewit, K. S. Colwell, W. A. Goddard and W. M. Skiff, *J. Am. Chem. Soc.* **1992**, *114*, 10024-10035

[34] L. D. Gelb and K. E. Gubbins, *Langmuir* **1999**, *15*, 305-308.

[35] C.S. Grange, A.J.H.M. Meijer, M.D. Ward, *Dalton Trans.* **2010**, *39*, 200.

[36] M. Hmadeh, Z. Lu, Z. Liu, F. Gándara, H. Furukawa, S. Wan, V. Augustyn, R. Chang, L. Liao, F. Zhou, E. Perre, V. Ozolins, K. Suenaga, X. Duan, B. Dunn, Y. Yamamto, O. Terasaki, O.M. Yaghi, *Chem. Mater.* **2012**, *24*, 3511.

[37] J. Rouquerol, P. Llewellyn, F. Rouquerol, F. Rodriquez-Reinoso, N. Seaton, *Stud. Surf. Sci. Catal.* **2007**, *160*, 49.

[38] M. Hmadeh, Z. Lu, Z. Liu, F. Gándara, H. Furukawa, S. Wan, V. Augustyn, R. Chang, L. Liao, F. Zhou, E. Perre, V. Ozolins, K. Suenaga, X. Duan, B. Dunn, Y. Yamamto, O. Terasaki, O.M. Yaghi, *Chem. Mater.* **2012**, *24*, 3511.

[39] N.T.T. Nguyen, H. Furukawa, F. Gándara, C.A. Trickett, H.M. Jeong, K.E. Cordova, O.M. Yaghi, *J. Am. Chem.*

Soc. **2015**, *137*, 15394.

[40] S. Geller, *J. Chem. Phys.* **1960**, *33*, 676.

[41] G. Socrates, *Infrared and Raman Characteristic Group Frequencies: Tables and Charts, Vol. 3*, Wiley & Sons Ltd., Chichester, **2001**.